

THE NIRSPEC BROWN DWARF SPECTROSCOPIC SURVEY II: HIGH-RESOLUTION J-BAND SPECTRA OF M, L and T DWARFS¹

IAN S. MCLEAN¹, L. PRATO², MARK R. MCGOVERN^{1,3}, ADAM J. BURGASSER⁴, J. DAVY KIRKPATRICK⁵, EMILY L. RICE¹ AND SUNGSOO S. KIM⁶

ABSTRACT

We present a sequence of high resolution ($R \sim 20,000$ or 15 km s^{-1}) infrared spectra of stars and brown dwarfs spanning spectral types M2.5 to T6. Observations of 16 objects were obtained using eight echelle orders to cover part of the *J*-band from 1.165-1.323 μm with NIRSPEC on the Keck II telescope. By comparing opacity plots and line lists, over 200 weak features in the *J*-band are identified with either FeH or H₂O transitions. Absorption by FeH attains maximum strength in the mid-L dwarfs, while H₂O absorption becomes systematically stronger towards later spectral types. Narrow resolved features broaden markedly after the M to L transition. Our high resolution spectra also reveal that the disappearance of neutral Al lines at the boundary between M and L dwarfs is remarkably abrupt, presumably because of the formation of grains. Neutral Fe lines can be traced to mid-L dwarfs before Fe is removed by condensation. The neutral potassium (K I) doublets that dominate the *J*-band have pressure broadened wings that continue to broaden from $\sim 50 \text{ km s}^{-1}$ (FWHM) at mid-M to $\sim 500 \text{ km s}^{-1}$ at mid-T. In contrast however, the measured pseudo-equivalent widths of these same lines reach a maximum in the mid-L dwarfs. The young L2 dwarf, G196-3B, exhibits narrow potassium lines without extensive pressure-broadened wings, indicative of a lower gravity atmosphere. Kelu-1AB, another

¹Department of Physics and Astronomy, UCLA, Los Angeles, CA 90095-1562; mclean@astro.ucla.edu

²Lowell Observatory, 1400 West Mars Hill Road, Flagstaff, AZ 86001

³Antelope Valley College, 3041 West Avenue K, Lancaster, CA 93536

⁴Massachusetts Institute of Technology, 77 Massachusetts Avenue, Building 37, Cambridge, MA 02139

⁵Infrared Processing and Analysis Center, MS 100-22, California Institute of Technology, Pasadena, CA 91125

⁶Department of Astronomy & Space Science, Kyung Hee University, Yongin-shi, Kyunggi-do 449-701, Korea; sskim@ap.khu.ac.kr

L2, has exceptionally broad infrared lines, including FeH and H₂O features, confirming its status as a rapid rotator. In contrast to other late T objects, the peculiar T6 dwarf 2MASS 0937+29 displays a complete absence of potassium even at high resolution, which may be a metallicity effect or a result of a cooler, higher-gravity atmosphere.

Subject headings: infrared: stars — stars: atmospheres — stars: low-mass, brown dwarfs

1. Introduction

With effective temperatures $\lesssim 2200$ K, the cool atmospheres of L and T dwarfs generate complex spectra that are rich in molecular features, especially at near-infrared (NIR) wavelengths where ro-vibrational transitions of many molecules dominate. Fortunately, these cool, very low luminosity objects are also brightest in the NIR. Until recently, most infrared spectroscopic investigations of L and T dwarfs have concentrated on the identification of strong, broad spectral features, useful for the establishment of spectral classification, and have employed resolving powers of $R = \lambda/\Delta\lambda \lesssim 2000$ (Burgasser et al. 2002, 2004, 2006; Cushing et al. 2003, 2005; Geballe et al. 1996, 2002; Jones et al. 1994; Leggett et al. 2000, 2001; McLean et al. 2000a, 2001, 2003a; Reid et al. 2000; Testi et al. 2001). Observations with significantly higher spectral resolution are potentially very important because line-blending from molecular transitions is reduced and weak features are resolved. Higher resolution spectra are more useful for constraining models of the complex molecular chemistry of brown dwarf atmospheres and for characterizing properties such as gravity and metallicity (Mohanty et al. 2004). For example, less massive brown dwarfs and younger brown dwarfs have smaller surface gravities which results in less pressure broadening and a different line shape. Furthermore, spectra with $R \gtrsim 20,000$ ($\lesssim 15$ km s⁻¹) are required for the measurement of radial and rotational velocities, and to search for radial velocity variability associated with brown dwarf spectroscopic binaries.

Obtaining high signal-to-noise observations with an increase in spectral resolution of a factor of ten is difficult because brown dwarfs are so faint. Basri et al. (2000) successfully

¹Data presented herein were obtained at the W.M. Keck Observatory, which is operated as a scientific partnership among the California Institute of Technology, the University of California and the National Aeronautics and Space Administration. The Observatory was made possible by the generous financial support of the W.M. Keck Foundation.

resolved the resonance absorption lines of Cs and Rb in the far-red visible regime for a sample of M and L dwarfs using the HIRES echelle spectrograph on the Keck 10-m telescope and derived effective temperatures through comparison with available model atmospheres. Reid et al. (2002) also used high-resolution optical echelle spectroscopy to study 39 dwarfs with spectral types between M6.5 and L0.5. However, because brown dwarf fluxes are significantly less in visible light, high-resolution observations of fainter L dwarfs and of the even dimmer T dwarfs are not tenable in the optical and require infrared observations. With the advent and development of sensitive large-format IR array detectors, IR spectroscopy with the requisite spectral resolution is now possible (McLean et al. 1998, 2000b).

In this paper we present the first well-sampled spectral sequence of late M, L and T dwarfs observed at high resolution ($R \sim 20,000$) in the NIR. This work is part of the NIR-SPEC Brown Dwarf Spectroscopic Survey (BDSS) being carried out at the Keck Observatory; preliminary results were presented in McLean et al. (2003b). The goals of the BDSS are to obtain a significant sample of NIR spectra of low-mass stars and brown dwarfs of differing ages, surface gravities, and metallicities at both medium ($R \sim 2,000$) and high spectral resolution for spectral classification studies and comparisons with model atmospheres. McLean et al. (2003a), hereafter M03, describes the lower resolution part of the survey; spectra from that study are available online.² Here, we investigate the *J*-band using ten times higher spectral resolution than in M03. The *J*-band (defined as 1.15-1.36 μm in this paper) is important because this region contains four strong lines of neutral potassium (K I) that are both temperature and gravity-sensitive, and which persist throughout the M, L, and T dwarf sequence. In §2 we describe our observations and data reduction procedures. §3 provides a discussion of the rich, spectral morphology. In addition to atomic K I, there are lines of Al I, Fe I, Mn I, Na I and Ti I, and transitions of molecular species such as CrH, FeH, and H₂O that can provide a unique resource for improving model atmospheres at these low temperatures. We show that the sudden disappearance of the Al I lines critically defines the M-L boundary at these resolutions. Concentrating on the strongly pressure-broadened K I lines, we look for correlations between spectral type and equivalent widths, velocity widths (FWHM), and residual intensity. The relation between molecular line strengths and spectral type is also investigated. The effects of rotation, surface gravity and metallicity are explored in §4. A summary of the overall results and concluding remarks is given in §5.

²<http://www.astro.ucla.edu/~mclean/BDSSarchive/>

2. Observations and Data Reduction

2.1. Targets and Instrumentation

Targets for the initial survey, the BDSS (M03), were selected primarily from well-known M dwarfs and from L and T dwarfs identified in the Two Micron All Sky Survey (2MASS; Kirkpatrick et al. 1997, 1999, 2000, 2001; Burgasser et al. 2000, 2002; Reid et al. 2000; Wilson et al. 2001), augmented with discoveries from the Deep Near-Infrared Survey of the Southern Sky (DENIS; Delfosse et al. 1997, 1999), the Sloan Digital Sky Survey (SDSS; Leggett et al. 2000; Geballe et al. 2002), and other investigations (Becklin & Zuckerman 1988; Ruiz, Leggett and Allard 1997). To ensure high signal-to-noise spectra for the high-resolution part of the survey, a subset of 12 of the brightest objects ($J = 7 - 15$), spanning the spectral type range from M6 to T6, was selected. Of these, only 2MASS 0140+27 was not part of the initial survey. The M2.5 star G196-3A was also observed along with its L2 companion G196-3B, both examples of objects substantially younger than 1 Gyr (Rebolo et al. 1998) and therefore most likely to exhibit gravity effects (McGovern et al. 2004). In addition, the peculiar T6 dwarf 2MASS 0937+29 (Burgasser et al. 2002) was added to the list because of its apparent lack of K I features in lower resolution spectra. Another late T dwarf (2MASS 2356–15, T5.5) was observed after completion of the initial set for comparison to the 2MASS 0937+29. Although the signal-to-noise ratio was sufficient to establish the presence of K I absorption in this T5.5 dwarf, the fainter magnitude ($J = 15.8$) and stronger H₂O absorption made quantitative analysis too difficult so the spectrum is not shown.

Table 1 provides the complete list of 16 targets and the observing log. Shorthand names such as 2MASS 1507–16 are used in the text for simplicity, but the full designations are listed in Table 1. Two targets were known visual doubles at the time of observing, 2MASS 0746+20 (L0.5) and DENIS 0205–11 (L7), but in neither case did we have sufficient angular resolution to separate the components. Subsequent to making our observations, DENIS 0205-11 was reported as a possible triple brown dwarf system (Bouy et al. 2005) based on Hubble Telescope images. Burgasser et al. (2005) subsequently found SDSS 0423–04 to be double, the average spectral type of T0 being due to an L6 and T2 combination. Even more recently, the binary nature of Kelu-1, a 0'29 pair, was revealed using Laser Guide Star adaptive optics on the Keck telescope (Liu & Leggett 2005; Gelino et al. 2006). Again, in neither case were these targets resolved in our NIRSPEC observations.

All of the observations were made using the NIRSPEC cryogenic spectrometer on the Keck II 10-m telescope on Mauna Kea, Hawaii. Detailed descriptions of the design and performance of this UCLA-built instrument are given elsewhere (McLean et al. 1998; 2000b).

For this study, NIRSPEC was used in its cross-dispersed echelle mode. High resolution spectra are dispersed across the 1024×1024 InSb detector at $0''.143$ per pixel while the spatial scale in the cross-dispersed direction is $0''.19$ per pixel. An independent slit-viewing camera with a scale of $0''.18$ per pixel is available for centering and guiding. With the gratings used in NIRSPEC, the relationship between the blaze wavelength (λ_b) and echelle order number (m) is $m\lambda_b = 76.56 \mu\text{m}$; together with the free spectral range (see below), this equation gives the order location of a given wavelength. The spectrometer was set up with the NIRSPEC-3 order-sorting filter and specific echelle and cross-dispersion grating angles to record 11 echelle orders ($m = 66$ to $m = 56$) covering the wavelength range from 1.15 – $1.36 \mu\text{m}$, corresponding approximately to the standard *J*-band. The free spectral range (λ_b/m) at $1.255 \mu\text{m}$ (order 61) is $\sim 206 \text{ \AA}$, but the effective dispersion is 0.179 \AA/pixel , allowing for only 183 \AA (89%) of this order to be captured by the detector. In fact, the captured wavelength range varies from 171 \AA (94%) in order 65 to 192 \AA (84%) in order 58. Thus, because the spectral interval captured by the detector is slightly smaller than the free spectral range in each order, there are small gaps, increasing with wavelength, in the total spectral coverage. Table 2 summarizes the spectral range for each order used in the subsequent analysis. In practice, for an entrance slit $0''.43$ (3 pixels) wide, the final spectral resolution in the reduced data is $R \sim 20,000$, (or 15 km s^{-1}), compared to the theoretical value of $R = 24,000$. The average value of one spectral resolution element is $\sim 0.625 \text{ \AA}$ (equivalent to 3.6 pixels) over most of the *J*-band region.

Spectroscopic observations were made as nodded pairs. Typically, integrations of 600 s each were taken with the object placed at two positions, designated A and B, separated by $\sim 7''$ on the $\sim 12''$ long entrance slit of NIRSPEC. Shorter exposure times were used for brighter objects. Exposures of 300 s per nod position were used for 2MASS 0746+2000AB, Kelu-1AB and 2MASS 1507-1627, 120 s for Wolf 359 and 60 s per nod position for G196-3A. Total integration times per object ranged from a few minutes to 1.5 hours depending on the apparent *J* magnitude. Signal-to-noise ratios were typically greater than 20 (5%) per resolution element over most orders, and sometimes greater than 100 (1% noise). Seeing conditions were $\sim 0''.5 - 0''.6$ and therefore a slit width of $0''.43$ (3 pixels) was used for all observations, except in the case of 2MASS 1507–16, for which we used a $0''.576$ (4 pixels) slit because of poorer seeing. A0 V stars were observed at an airmass very close to that of the target object to calibrate for absorption features caused by the Earth’s atmosphere. Arc lamp spectra, taken immediately after each observation, and OH night sky lines in the observed spectra, were used for wavelength and dispersion calibration. A white-light spectrum and a corresponding dark frame were obtained for flat-fielding.

2.2. Data Reduction Methods

For the data reduction we used REDSPEC, an IDL-based software package developed at UCLA for NIRSPEC by S. Kim, L. Prato, and I. McLean³. For each echelle order, REDSPEC uses the position of the two-dimensional spectra on the NIRSPEC array and the calibration line spectra to construct spatial and spectral maps necessary to transform the raw data onto a uniform grid. If the target spectrum itself is too faint to provide the spatial rectification, then the A0V star observed with the same set up was used instead. Although four arc lamps are available, it is often the case that there are too few well-distributed lines per echelle order for good spectral rectification. Consequently, OH night sky lines were also used. The dispersion was more than adequately fit by a second order polynomial of the form $\lambda = c_0 + c_1x + c_2x^2$ where $c_1 \sim 0.17 \pm 0.01 \text{ \AA/pixel}$ and $c_2 \sim 7 \times 10^{-6} \text{ \AA/pixel}^2$. To extract spectra free from atmospheric background and uneven detector response, the difference of an A/B image pair was formed and flat-fielded. The flat-fielded difference frame was then rectified using the spatial and spectral maps and the raw spectrum produced by summing 5–10 rows from each trace in the rectified image. The extracted traces (one positive, one negative) are subtracted again to produce a positive spectrum with residual night sky emission line features removed, unless a line was saturated. In the *J*-band, none of the night sky emission lines are saturated. A0 V star spectra were reduced in the same way, interpolating over the intrinsic Pa β hydrogen absorption line at $1.28\mu\text{m}$ in the *J*-band spectra. The raw target spectrum was then divided by the raw A0 V star spectrum to remove telluric features. The true slope of the target spectrum was restored by multiplication with a blackbody spectrum of $T_{eff} = 9500 \text{ K}$ for an A0 V star (Tokunaga 2000). Finally, the spectra reduced from multiple A/B pairs were averaged together to improve the signal-to-noise ratio.

3. J-band Spectral morphology at $R \sim 20,000$

3.1. Overview

For each of the 16 targets we have extracted 8 echelle orders (see Table 2) yielding a total of 128 spectra. Before examining and interpreting the new spectra in detail, it is very useful to have a broad overview of the basic spectral features present and an awareness of the general trends that occur in the high-resolution *J*-band data as a function of spectral type. A convenient way of doing this is to select a representative source for a few spectral types and present all eight echelle orders on the same plot, thus enabling the entire *J*-band

³See <http://www2.keck.hawaii.edu/inst/nirspec/redspec/index.html>

to be viewed at a glance. Figures 1–6 show the reduced spectra of Wolf 359 (M6), 2MASS 0140+27 (M9), 2MASS 0345+25 (L0), 2MASS 1507–16 (L5), SDSS 0423–04AB (T0) and 2MASS 0559–14 (T4.5). The double nature of SDSS 0423–04AB means that we do not have a true T0 spectrum, but lower resolution studies (M03) show that J-band spectral variations are relatively weak from L6 to T2 and therefore this binary remains a useful proxy for a T0 dwarf. In these plots, echelle orders 58 through 65 are shown together; the remaining orders at the edges of the *J*-band are too contaminated by strong atmospheric absorption to be useful. For ease of comparison, all spectra are shown in the laboratory reference frame and vacuum wavelengths are used throughout; radial velocities and searches for radial velocity variations will be reported and discussed in a separate forthcoming paper (Prato et al. 2006 in prep.). Each order is normalized to unity at the same wavelength. Comparison of the spectra in these six figures, all of which have excellent signal to noise ratios (at least 20:1 per pixel), shows that the region is densely populated with numerous weak absorption features and a few stronger lines. We will show that the fine-scale spectral structure is real and repeatable, and that it is mainly attributable to FeH or H₂O. The strongest atomic features are the doublets of K I that occur in orders 61 and 65. These lines persist from M6-T4.5 but clearly change their character with spectral type. In later sections the K I lines will be singled out for closer inspection. For reference, Table 3 summarizes the main spectral transitions observed in the *J*-band over the spectral type range from M6-T4.5, including the energy levels of the atomic transitions.

As shown in Figure 1, the M6 dwarf Wolf 359 has at least one distinguishing feature in each order. Atomic lines of Al I at 1.31270 and 1.31543 μm appear in order 58. There is a moderately strong line of Mn I at 1.29033 μm in order 59, plus some weaker lines of Ti I at 1.28349 and 1.28505 μm . A weak unresolved Na I doublet is seen at 1.26826 μm in order 60. The first pair of strong K I lines at 1.24357 and 1.25256 μm appears in order 61. Multiple weak absorption features occur in both orders 62 and 63, the most notable grouping being the set of lines around 1.222 μm . Several of the stronger features have been identified with FeH from lower resolution studies (Jones et al. 1996; Cushing et al. 2003; M03). Note however, that a major FeH band head at 1.24 μm is just off the detector at the short wavelength edge of this order. In order 64 there is a pair of strong Fe I lines at 1.18861 and 1.18873 μm and another Fe I line at 1.19763 μm . Order 65 contains the second set of strong K I lines, one at 1.169342 μm and the close pair at 1.177286, 1.177606 μm . In general, the lines are relatively sharp and well-resolved. Wolf 359 is a bright source and therefore the signal-to-noise ratio in this spectrum is at least 100:1.

Following these spectral features order by order through Figures 1-6 reveals certain general trends as a function of spectral type. Comparing the M9 object (Figure 2) with the M6 source (Figure 1) we see that the Al I lines at 1.3127 and 1.3154 μm in order 58 are

somewhat weaker at M9 and then suddenly they are no longer present at L0 (Figure 3), or in any later spectral types (Figures 4-6). This is an important observation that relates to the M-L transition and we will discuss the Al I lines in the next section. Throughout order 58 there are other weaker spectral features, the so-called fine-scale spectral structure. This spectral structure becomes more pronounced at M9 (Figure 2), seems broader in the L0 and L5 objects (Figures 3 and 4), weakens at T0 or more accurately from L6 to T2 (Figure 5) and then completely changes character by T4.5 (Figure 6). The most likely interpretation of this spectral sequence is that it represents changes in the physical structure of these cool atmospheres (temperature, pressure, chemistry). In subsequent sections we compare opacity data for different molecular species to identify the primary absorbers at each spectral class.

In order 59 the sharp Mn I line at $1.2903 \mu\text{m}$ seen at M6 and M9 (Figures 1 and 2) broadens and disappears after L0 (Figure 3). The fine-scale spectral structure in this order is dominant until T0 composite type (Figure 5) when the spectrum becomes remarkably smooth. Here again the high resolution data reveal a striking effect, this time at the transition from L to T dwarfs. New spectral structure develops in this order between types T0 at T4.5 (Figure 6) but, as was the case for order 58, the pattern is different, indicating different atmospheric conditions.

The weak Na I line at $1.2683 \mu\text{m}$ detected in order 60 in the M6 object (Figure 1) is already absent in the M9 object (Figure 2). Otherwise, the behavior of the fine-scale structure follows a pattern similar to order 59 becoming remarkably weak at T0 (Figure 5) and leading to a smoother appearance for these spectra near the L-T transition.

Order 61 contains one of the pairs of strong K I doublets located at 1.2436 and $1.2525 \mu\text{m}$. These lines deepen and widen slightly from M6 to M9, and then become increasingly broader and shallower from L0 to T4.5. NIRSPEC spectral order 61 also has many fine-scale features attributable to molecular transitions. Two features, one at 1.24637 and the other at $1.24825 \mu\text{m}$ have been identified previously with FeH (Cushing et al. 2003). These FeH lines strengthen slightly from M6 to M9 (Figures 1 and 2), become much broader in the L dwarfs (Figures 3 and 4) and then vanish completely in the T dwarfs (Figures 5 and 6) to leave, once again, a remarkably smooth continuum between the K I lines.

Comparing orders 62 and 63 in Figures 1-6, the known FeH features in these spectral bands strengthen from M6 to M9, broaden markedly at L0 and remain strong and broad through L5 before becoming weaker in the T0 and T4.5. As with the atomic lines, the individual FeH lines seem to broaden significantly at the transition from spectral types M9 to L0. Evidence of weak FeH absorption is still present around $1.222 \mu\text{m}$ at spectral type T0, and possibly even at T4.5, as shown in Figures 5 and 6, but this molecular species is clearly not dominant in T dwarfs.

For the M6 dwarf (Figure 1), order 64 is characterized by a pair of strong lines of Fe I at 1.18861 and 1.18873 μm that are easily resolved, and another Fe I line at 1.19763 μm that is blended with FeH. These features remain strong at M9 (Figure 2) and persist into the L-dwarf range, becoming broader at L0 (Figure 3), and then undetectable by L5 (Figure 4). From T0 to T4.5 (Figures 5 and 6), order 64 becomes increasingly chopped up by new spectral features, some of which are quite sharp and deep. In section §3.3 we show that these features are caused by absorption by H₂O.

Finally, there is order 65, which contains the second K I doublet and exhibits some of the largest changes with spectral type. The slightly weaker K I companion line at 1.17728 μm , only 3.3Å from the longer wavelength member of the doublet is easily resolved in the M9 object (Figure 2), already blended from line broadening in the L0 (Figure 3), barely discernable at L5 (Figure 4), and completely washed out by line broadening and numerous molecular features at T4.5 (Figure 6). Order 65, being close to the short wavelength edge of the *J*-band where terrestrial water vapor absorption is expected, also contains many strong intrinsic transitions of hot H₂O, for example, the feature at 1.175 μm .

3.2. Al I, Fe I and Mn I; indicators of the M-L transition

Figure 7 provides a more detailed view of the Al I doublet in order 58. In this plot, the spectra for the M6, M9 and L0 objects shown in Figures 1-3 are expanded and overlaid. Evidently, there is significant spectral structure in this part of the spectrum making it difficult to identify a true continuum level. All three spectral types show consistent features, in particular the wide depression containing the shorter wavelength Al I line. The equivalent width of the Al I lines clearly decreases from M6 to M9, but the change over these three spectral types is only about 25%. Because this region of spectrum is contaminated by H₂O absorption, it is difficult to obtain accurate equivalent widths. A pseudo-equivalent width over a 4.2Å interval centered on each line was obtained relative to the local continuum in the troughs where the Al I lines are found. For the stronger line of the pair at 1.3127 μm , the measured values of equivalent width for the M6 and M9 dwarfs respectively are 420 ± 20 mÅ and 300 ± 40 mÅ. At L0, however, the pseudo-equivalent width of this line is ≤ 40 mÅ. Clearly, at the transition from M9 to L0, both Al I lines vanish completely. Although only three objects bridging this transition were observed at high resolution, the conclusions given here are supported fully by the results of our low resolution BD spectroscopic survey (M03) where two objects of every spectral type from M6 to L5 was included.

As shown in Table 3, these lines arise from absorption from an energy level at 3.14 eV. Interestingly, the Na I line at 1.268 μm in order 60 is already absent in the M9, and

careful inspection shows that a somewhat broadened Mn I line at $1.290 \mu\text{m}$ in order 59 persists through L0. The Na I line is excited from a high energy state at 3.6 eV whereas the Mn I line comes from a state at only 2.1 eV. Thus, the sequence in which the lines disappear is at least qualitatively consistent with thermal excitation. But the abrupt loss of Al I lines at the classical M-L boundary is too great to be explained by Boltzmann factors alone. For example, for a temperature change from 2850 K from the M6 to about 2400 K for the M9 say, the population of excited atoms in the upper level would drop by 51% and the equivalent width of the line might change from $420 \text{ m}\text{\AA}$ to about $210 \text{ m}\text{\AA}$ if all other factors remain the same. From M9 to L0 the change would be a further 13% assuming a change in effective temperature of 150 K. Thus, the line should still be measurable with an equivalent width of $140 \pm 40 \text{ m}\text{\AA}$, or about one-third its value at M6. Yet, both lines disappear abruptly. It is likely, from the models of Lodders (2002), that aluminum has been sequestered in compounds such as hibonite ($\text{CaAl}_{12}\text{O}_{19}$) and that this abrupt change in absorption line strength is really caused by the sudden depletion of aluminum as an absorber due to a significant change in atmospheric chemistry, rather than simply a drop in effective temperature. Gas temperatures typical of this transition are near 2000 K (Lodders 2002).

It is also curious that the intensity ratio of the components of the Al I doublet is closer to 3:2 than the expected 2:1 ratio based on their statistical weights. However, as shown in Figure 7, this spectral region is highly complex with many overlapping transitions which makes it difficult to determine the true continuum level for each line. Alternatively, the peculiar line ratios may be a non-LTE effect, or the result of line blending.

Another element that is also important for understanding the temperature structure of these cool, dust-forming objects is iron. As previously mentioned, order 64 contains a remarkably strong pair of Fe I lines at 1.1886 and $1.1976 \mu\text{m}$. The shorter wavelength Fe I line is a resolved double with a separation of 1.2\AA in the M6 and M9 objects, but appears as a single broad feature at L0. By L5 the Fe lines are completely absent. Lower resolution studies (M03) also suggested that Fe disappeared around L2 or L3. These Fe I lines arise from low-lying energy levels near 2.2 eV, and gas phase iron requires temperatures above about 1700 K (Burrows et al. 2001). Combining the results that Al disappears at L0 and Fe is no longer present by L3, and using the chemistry temperature scale, suggests that there is about a 300 K temperature change from L0 to L3, which is shallower but still consistent with the interval of about 140 K per spectral type derived by Burgasser et al. (2002) as well as the effective temperature scale of Golimowski et al. (2004). As noted by Burgasser et al. (2002), temperatures derived from condensation chemistry tend to be systematically cooler by about 500 K than those derived from empirical determinations of T_{eff} using objects with known parallax. These conclusions are not necessarily inconsistent if different spectral features probe a range of optical depths in the atmosphere.

Finally, we note the presence of several weak lines of Ti I that arise from energy states near 1.4 eV, even lower than those of the strong potassium lines. A strong Ti multiplet at 0.97 μm has also been seen in the spectra of M dwarfs up to at least M9 (Cushing et al. 2005). Unfortunately, these weak lines are impossible to trace after M9.

3.3. Fine-scale structure; the role of FeH and H₂O

The astronomical *J*-band is bounded by H₂O absorption bands from terrestrial water vapor. It is therefore no surprise that high-temperature H₂O (hot steam) transitions intrinsic to M, L and T dwarfs encroach far into the *J*-band from both the short and long wavelength ends. These so-called infrared water bands are difficult to model because millions of transitions are needed (Partridge & Schwenke 1997). Typically, models over-estimate the depth of the infrared water bands. In addition to H₂O, some of the stronger non-atomic transition features are known to be attributable to FeH from lower resolution studies (Jones et al. 1996; McLean et al. 2000). These features occur at 1.2091, 1.2113, 1.2135 and 1.2221 μm . Cushing et al. (2003) verified the features at 1.1939 and 1.2389 μm as the 0–1 and 1–2 band heads of the F⁴ Δ – X⁴ Δ system of FeH, and attributed a blended feature described by McLean et al. (2000) at 1.2221 μm as the F⁴ $\Delta_{7/2}$ – X⁴ $\Delta_{7/2}$ Q-branch. These authors also listed 24 other relatively strong features lying within the *J*-band. In the Cushing et al. list, no FeH features were identified in the wavelength interval covered by our order 65, which includes the strong shorter-wavelength doublet of K I, and only one feature (at 1.2464 μm) was tabulated for order 61, where the other K I doublet dominates.

To identify many more of the complex fine-scale features seen in the spectral sequences of Figures 1–6, we analyzed opacity (cross-section) data for both FeH and H₂O, (R. Freedman 2003, private communication) and utilized the FeH line list and transition catalog by Phillips et al. (1987). We are also grateful to Adam Burrows who provided CrH opacity data (Burrows et al. 2002) and Linda Brown who provided new opacity calculations for CH₄ in the *J*-band (L. Brown 2004, private communication).

Figure 8 is a detailed view of order 62 (1.221–1.239 μm) for the M9 object 2MASS 0140+27. Superimposed on the M9 dwarf spectrum is a normalized and scaled FeH opacity plot for a temperature of 2000 K and a pressure of 1 bar. We use this plot to assist in identifying spectral features. This interesting region of the *J*-band contains a feature which is seen in lower resolution spectra as a broad, flat-bottomed line at 1.2221 μm (McLean et al 2000a). Each transition in the opacity data can be correlated with either 0–1 or 1–2 transitions of the F⁴ Δ – X⁴ Δ system tabulated by Phillips et al. (1987). As shown in Figure 8, the feature observed at 1.2221 μm and attributed to the Q-branch by Cushing

et al. (2003), is actually a composite of four Q-branch and three P-branch transitions plus one R-branch transition of FeH. Thus, at our higher resolution, the broad flat-bottomed feature seen in lower resolution spectra is completely resolved into eight separate transitions. These transitions are the following: Q(0-1) at 1.22137 and 1.221383 μm blended, 1.221934, 1.222504 and 1.22305 μm ; P(0-1) at 1.22166, 1.22219 and 1.22244 μm ; R(0-1) at 1.22218 μm . R-branch transitions tend to correspond closely to P-branch lines. For example, the P(0-1) 1.22219 μm line is only 0.1 \AA from the R(0-1) transition just given. Also, the Q-branch line at 1.222504 μm is blended with the nearby P-branch transition at 1.22244 μm .

The remainder of order 62 is dominated by 5 R-branch lines and about 30 P-branch transitions; all are members of the $F^4\Delta - X^4\Delta$ system. In this one order alone, there are now more identified FeH transitions than previously known for the entire J -band. Summing up across all NIRSPEC orders, we identify over 200 matches to the FeH opacity data base and the tables by Phillips et al. (1987). There is little doubt that FeH is a dominant molecular absorber in late M and early L spectral types.

Interestingly, there are several features that cannot be identified with FeH transitions in the given opacity tables. For example, a sharp line at 1.2227 μm contaminates the Q-branch feature, and there are other isolated groups near 1.225, 1.228, 1.231 and 1.234 μm which also are not attributable to FeH. Because these features have a dependence on spectral type that is similar to FeH, they may be unknown FeH transitions or transitions of CrH. To explore the latter possibility we also compared our spectra to CrH opacity calculations by Burrows et al. (2002). Although the CrH opacity data had a lower resolution than our spectra, there was good coincidence for the features at 1.225, 1.228 and 1.231 μm , but the features near 1.234 μm could not be identified with CrH. Although transitions of CrH contaminate those of FeH, the strongest fine-scale features in this part of the J -band are attributable to FeH rather than CrH. Stronger CrH bands occur at shorter wavelengths (Kirkpatrick et al. 1999).

We also investigated the fine-scale structure in orders 61 and 65 which contain the important K I doublets. Figure 9 provides a plot of the FeH opacity (at 2000 K and 1 bar pressure) across order 61, normalized for convenience, smoothed to match the resolution of our spectra, and over-plotted with the spectra of our M9 and L5 dwarfs. Essentially every feature can be traced to FeH, with a few notable exceptions. For example, absorption features at 1.2448 and 1.2458 μm are clearly associated with FeH, but two significant absorptions bands in between these limits do not correlate with FeH. Note also that the L5 spectral features are broader than the equivalent features in the M9 object.

As shown in Figures 1-6, there is a general increase in the strength of FeH from mid-M until about L4 and then a decrease in FeH features towards later spectral types. Figure 10 shows a plot for order 61 in which the L5 and the T4.5 dwarfs in our sample are compared.

In this figure H₂O opacity curves (at 1000 K and 1 bar) are over-plotted. The T4.5 spectrum lacks FeH, and its shallow depressions and small features are consistent with the H₂O opacity. The FeH feature near 1.245 μm appears strongest in the early to mid Ls, while the H₂O transition at 1.1752 μm seems to gain in strength systematically toward later spectral types.

In order 65, no transitions for FeH are listed in the opacity files at the shorter wavelengths. Therefore, in Figure 11, we plot the H₂O opacity (at 1000 K and 1 bar) for order 65, and over-plot with the spectrum of the L3.5 and T4.5 from our sample. This pair of spectral types provides distinct morphological samples. Most of the features in the T4.5 dwarf evidently correspond to H₂O. There is a particularly strong H₂O feature at 1.1752 μm in the T4.5 dwarf, which is also present in the L3.5 object at a weaker level. In fact, weak H₂O absorption is already present even in late M objects.

We also looked for transitions associated with the ϕ bands of TiO (Galehouse 1980; Phillips 1973). These bands have been detected in young, low-gravity sub-stellar objects by McGovern et al. (2004), but are not usually apparent in low resolution spectra of older field dwarfs. A model spectrum kindly provided by D. Saumon shows the location of numerous ϕ -band transitions in order 61, with noticeable band heads for the $\Delta\nu=-1$, (0-1) and (1-2) transitions at 1.25644 and 1.24239 μm respectively. Absorption features do occur at these wavelengths from M6-L5, but these also coincide with FeH features and are less likely to be TiO because none of the other TiO transitions of the ϕ band are seen.

Finally, using new opacity data for CH₄ (L. Brown 2004, private communication), we searched for evidence of methane transitions in the T dwarfs. The strongest features should occur in order 65 which also contains the very broad shorter-wavelength K I doublet. Unfortunately, this spectral region is already heavily blanketed by H₂O absorption. Even in the high signal-to-noise spectra of 2MASS 0559-1404 (T4.5), there are no transitions that can be uniquely attributed to CH₄.

3.4. The potassium doublets

Because the K I doublets dominate orders 61 and 65, and because these strong lines clearly persist throughout almost the entire M, L and T range, we plot 12 of the objects from Table 1 together in Figures 12 and 13 to provide a more continuous sequence for these features. For this figure, the L4 GD165B has been left out because the L3.5 2MASS 0036+18, with better signal-to-noise ratio, has been included; GD165B will be discussed separately. The other two objects omitted from these plots are the peculiar L2, G196-3B, and the peculiar T6 dwarf, 2MASS 0937+29; again, these objects are discussed separately

later. Each spectrum in Figures 12 and 13 has been normalized to a continuum value of one at a common wavelength and shifted for clarity by an additive constant along the y-axis. The spectra have been ordered according to their published classification (Optical types for L-dwarfs: Kirkpatrick et al. 1999, 2000, 2001; NIR for T dwarfs: Burgasser et al. 2006) and aligned at the K I rest wavelengths in vacuum. As mentioned already, radial velocity determinations will be presented in a separate paper (Prato et al. 2006, in prep.).

As given in Table 3, the shorter wavelength K I lines (in order 65) correspond to the multiplet designation $4p\ ^2P^o-3d\ ^2D$, and the order 61 pair to the $4p\ ^2P^o-5s\ ^2S$ multiplet. All are transitions between states at 1.61–2.67 eV. The pair of K I lines in order 65 have almost equal intensity at the line center, whereas in order 61, the 1.2436 μm line is always weaker than the 1.2526 μm line. For both K I doublets, the line ratios are similar throughout the spectral sequence.

One of the most prominent results, evident in both Figures 12 and 13, is the significant K I line broadening in the later type objects. Primarily because of its higher temperature, the M2.5 dwarf manifests very narrow lines with almost no wings. There is a slight contamination of the shortest wavelength K I line in order 65 from an Fe I line for spectral types before L4. For the M2.5, M6 and M9 dwarfs, separate peaks are clearly discernable for the longer wavelength line of the K I doublet in order 65 at 1.17761 μm and the secondary K I line at 1.17728 μm , but for later spectral types the 1.17761 μm lines are heavily blended and not discernable as separate features. In the earlier type objects, the pair of lines near 1.1786 μm in order 65 are attributable to Ti and Fe.

4. Analysis and Discussion

4.1. Correlating spectral features and spectral type

To quantify the changes in the K I lines illustrated in Figures 12 and 13 as a function of spectral type we calculate three quantities, a line depth, a line strength (equivalent width) and a line width. Line depth is defined in terms of the measured flux (F_λ) at the line center compared to the average value for the continuum. For convenience we construct the line depth as $1 - F_{line}/F_{cont}$ at the line center; a weak line has almost the same flux in the line as in the continuum and its line depth measure is therefore almost zero. Deep lines have a depth index approaching unity. Determining the continuum or pseudo-continuum level introduces the largest uncertainty into this ratio. The continuum is estimated by fitting a sloping line across the feature between the highest points on either side lying within $\pm 50\text{\AA}$ of the line center. Multiple trials obtained by varying the positions by a few Angstroms provide a mean

value and an estimate of the uncertainty from fluctuations in the continuum level.

Equivalent width (in Å) is also determined by fitting a continuum line between two points on either side of the line, summing the residual intensities and multiplying by the width of a pixel. The same range and method is used as for the line depth. Line width (in km s^{-1}) is defined as the full width of the line at the intensity level halfway between the apparent local continuum, defined above for the line depth and equivalent width, and the minimum line intensity at the line center (FWHM).

Several sources contribute to the uncertainty in the derived quantities. The continuum level is difficult to identify, photon noise reduces the signal-to-noise ratio for the fainter sources, and contamination by numerous weak features is dependent on spectral type. Molecular line contamination results in additional fluctuations in the measured K I quantities and gives larger uncertainties, despite the good signal-to-noise ratio of most of the spectra. Our final plotted uncertainties are based on repetitive trial fits and photon noise estimates.

Table 4 and Table 5 provide the measured quantities for the 1.2525 and 1.2436 μm K I lines respectively. This pair of K I lines (order 61) is preferred because the shorter wavelength doublet is too heavily contaminated by H_2O absorption, and one of the K I lines is itself a blend (§3). Figures 14, 15, and 16 show, respectively, the line depth, equivalent width and velocity line width as a function of spectral type for the 1.2525 μm line.

Several of the trends mentioned in the previous section are confirmed. The K I line depth increases from a weak line in early M dwarfs to a strong deep line in the early/mid L dwarfs before decaying towards later spectral types. Interestingly, there is considerable scatter in line depth among similar spectral types. The equivalent width (designated by W) is better behaved. Variations in defining a consistent continuum may have a large effect on the line depth quantity, whereas the growth of the line wings may overcome such variations when calculating W and FWHM. Equivalent width increases to a broad maximum around L2-L4 and then decreases again, remaining essentially constant from L5 - T4.5. These results are consistent with our more extensive lower resolution studies (M03). In contrast, the velocity line width of the 1.2525 μm K I line (Figure 16) increases almost monotonically and steeply with spectral type. The change in velocity width is dramatic, ranging from $\sim 60 \text{ km s}^{-1}$ at M6 to almost 500 km s^{-1} at T4.5. This change does not result from rotational broadening because the line develops extensive wings characteristic of pressure broadening as discussed in the next section. One L-dwarf appears to stand out from the others in this sequence and is indicated by a star symbol. This object is Kelu-1AB, and will be discussed separately in the next section. The behavior of the 1.2436 μm K I line (Table 5) is similar.

The changing behavior of the K I lines can be explained as follows. As the temperature

decreases towards later spectral types, the transition levels become less populated and the line should become weaker. However, with decreasing temperature, dust grains settle below the photosphere and the transparency of the atmosphere at wavelengths where gas opacity is weak improves. Thus, line formation can be observed at much greater depths and pressures (Saumon et al. 2003). Higher pressures cause the development of the broad line wings through collision broadening, primarily with H₂ molecules (e.g. Burrows & Voloyubev 2003), and hence an increase in the FWHM of the lines. The greater column depth of K I in these transparent regions also serves to increase their equivalent widths. The behavior has been observed with the K I and Na I fundamental doublets (Reid et al. 2000), and is one of the unique properties of brown dwarf atmospheres. The pressure broadening of the K I lines at J-band follow quantitative expectations as well. The observed ratio between the K I line widths in the T4.5 and L5 spectra is about 2:1. As the T_{eff} decreases, the pressure at $\tau=2/3$ increases as already described. According to models of cloudy atmospheres, kindly provided by D. Saumon (2003; private communication), the change in the photospheric pressure at these wavelengths is a factor of 5 from 1600 K to 1000 K. These effective temperatures were chosen to illustrate a prediction of the models over the typical range of L/T spectral types. This implies that the average kinetic energy of the molecules of H₂ is five times greater, or that the average speeds are ~ 2.24 times larger. Pressure broadened line widths should be proportional to the average velocity of the disturbing atoms. Thus, the observed pressure broadening from L5 to T4.5 is consistent with the expected change.

In contrast to the K I lines, Figures 17 and 18 show the changing trends with spectral type for two representative FeH and H₂O features that fall within the orders containing the K I doublets; data are provided in Table 6. For FeH we plot the line depth index of the 1.245 μm feature in order 61, and for H₂O we use the strong 1.175 μm feature in order 65. The FeH line depth reaches a peak around L3-L4, whereas the H₂O line depth increases more-or-less monotonically from M6 to T4.5. Once again Kelu-1AB stands out, this time because the FeH bands are not as deep as expected for an L2.

4.2. Line shapes: rotation and pressure broadening effects

In the previous section we found that the K I line width (FWHM) and the H₂O line depth provided the best correlations with spectral type. The exception to the FWHM correlation is Kelu-1AB, which *is* known to be a rapid rotator (Basri et al. 2000), and which was recently discovered to be a $\sim 0''.3$ visual binary (Liu & Leggett 2005; Gelino et al. 2006), although the orbital velocity of 3 km s⁻¹ is only a fraction of the $V \sin i$. As will be shown below, the K I lines are not really suitable for $V \sin i$ studies.

Interestingly, Kelu-1AB is not abnormal in its H₂O ratio. The one point in the H₂O plot of Figure 18 that does seem slightly high is due in fact to GD165B (L4); this result is consistent with M03. As the companion to a white dwarf, GD165B is most likely to be an old L dwarf with a higher gravity. Burgasser et al. 2003 has shown that late-type subdwarfs, which are also presumably older and have higher surface gravities, can show stronger H₂O compared to equivalently classified disk dwarfs.

The presence of a binary companion can impact the observed line properties discussed above in several ways. For example, a spectroscopic companion only partially resolved in velocity space might produce a spectrum with anomalously broadened lines at certain epochs. A spectroscopic companion of similar mass to the primary object should not only manifest itself in broadened lines, observed at a favorable phase, but also should almost double the expected brightness of the system. Fainter companions, although interesting in their own right, should not significantly impact the primary dwarf spectrum if the mass ratio, M_2/M_1 , is less than ~ 0.5 (Prato et al. 2002). Visual companions at separations too great to noticeably effect the spectrum will also cause the observed spectrum to appear brighter than expected for the distance and age of the target system. Four targets in Table 1 are visual binaries: 2MASS 0746+20 (L0.5), Kelu-1 (L2), DENIS 0205–11 (L7) and SDSS 0423–04 (T0). Signatures of velocity variations in these spectra will be addressed in a forthcoming publication.

Spectral features in Kelu-1AB appear to be significantly broader than other field dwarfs of similar temperature by a factor of 2-3, consistent with its high rotational velocity of 60 ± 5 km/s (Basri et al. 2000). In Figure 19 we compare the L2 dwarf, Kelu-1AB, with the L0.5 and L3.5 dwarfs in our sample. Because no feature is completely free of blending at this spectral resolution and wavelength throughout the late M to T sequence, measuring precise rotational velocities is challenging. Indeed, because of the increasing complexity of molecular features with cooler effective temperatures, most if not all of the lines in the mid-L to T objects may be blends. However, the wealth of fine-scale spectral structure attributable to FeH and H₂O throughout the *J*-band does provide some possibility of detecting trends in $V \sin i$, especially because pressure broadening should not be a large effect for molecular transitions.

Examining the rich FeH structure in order 61 (Figure 12), as well as orders 62 and 63 (Figures 1-4) where there are no strong alkali lines, it is clear that there is a sudden broadening of the FeH lines at the transition from M9 to L0, and that all of the FeH features remain broad after that transition. In fact, if the M9 spectra in orders 62 and 63 are smoothed by a factor of 3 using a simple moving average, the resulting spectrum is a very good match for the observed L0 spectrum. This sudden broadening could be caused by either increased

pressure broadening or an increase in rotational velocities. Examination again of Figure 13 shows that many of the H₂O spectral features that develop in the T dwarfs are relatively sharp, indicating that they are not formed at the same depth and pressure as the potassium line wings. Therefore, in the coolest objects, we are seeing evidence of vertical structure in the atmosphere. Like the FeH lines in the late M and early L dwarfs, the H₂O features provide a better estimate of rotational velocities than the alkali lines. We can de-convolve the instrumental profile by using the observed widths of unresolved OH night sky lines and the very narrow features seen in the M2.5 object. If we interpret the change in line width at the M9-L0 boundary as a rotational velocity, then after removal of the instrumental profile, all of the early L dwarfs appear to be rapid rotators with $V \sin i \gtrsim 30 \text{ km s}^{-1}$.

Rotational velocities have been reported for some of the objects in our target list. Basri et al. (2000) give $V \sin i = 60 \pm 5 \text{ km s}^{-1}$ for Kelu-1AB and $22 \pm 5 \text{ km s}^{-1}$ for DENIS 0205–11AB and $\lesssim 3 \text{ km s}^{-1}$ for Wolf 359 (Gl 406). The L3.5 dwarf 2MASS 0036+18 is reported to have a $V \sin i$ of $\sim 15 \text{ km s}^{-1}$ by Schweitzer et al. (2001). Several of our targets were also observed by Zapatero Osorio et al. (2006) at high resolution, enabling them to measure the $V \sin i$ of 2MASS 0036+18, SDSS 1254-01, and 2MASS 0559-14. We note with interest that the rotational velocities they measure for these sources, as well as for another dozen dwarfs, are all very close to 30 km s^{-1} within the uncertainties. We will analyze in detail the rotational velocities of our sample in a future paper; however, we comment here that our Figures 12 and 13 suggest that the T0 and T4.5 dwarfs in our sample, SDSS 0423-04 and 2MASS 0559-14, appear to reflect larger values of $V \sin i$. If there is a tendency towards more rapid rotation among the T dwarfs, it is not apparent in the measurements of Zapatero Osorio et al. (2006).

Clarke et al. (2003) report time resolved spectroscopy of Kelu-1AB used to search for variability in photospheric molecular species. They confirm the short rotation period of the system and find variable H α profiles. No evidence for a spectroscopic companion was detected and it appears to be a normal L dwarf apart from the high rotation rate (Clarke et al. 2003). The recently discovered 0.29" binary contributes only about 3 km s^{-1} in velocity shift and therefore has no impact on the measured $V \sin i$. However, it is interesting to ask whether or not both components have the same $V \sin i$. In the binary system Gl569B (Zapatero Osorio et al. 2004), line broadening is 2-3 times greater in one component than the other, although this has been attributed to a nested spectroscopic binary (Simon et al. 2006). It is possible that the higher rotation rate of Kelu-1AB is the result of age. A younger L dwarf just past the accretion phase might have a higher rotational velocity. On the other hand, as discussed in the next section, the young L2 dwarf G196-3B does not have such a rapid rotation, or is being viewed at a special angle.

4.3. Surface gravity effects

As shown by models (e.g. Burrows et al. 2001), the youngest brown dwarfs are expected to be hotter and more luminous. As a sub-stellar mass object cools over the first 100 Myr, its radius will contract by a factor of 2-10, depending on initial mass, and then remain almost constant at a value close to that of Jupiter’s radius. Consequently, a very young low-mass brown dwarf could be observed with a much earlier spectral type than it will have when older than 1 Gyr, and its surface gravity ($g = GM/R^2$) will be less than that of an old brown dwarf with the same observed spectral type. A lower surface gravity implies less pressure broadening ($P \sim g/k_r$, where k_r is the Rosseland mean opacity) and therefore one expects the K I lines to be narrower in such objects. The effect of surface gravity on the K I lines is significant and has already been observed at lower resolution (McGovern et al. 2004; Kirkpatrick et al. 2006). High resolution infrared spectroscopy of brown dwarfs provides a means of measuring surface gravities and hence estimating mass. Because of their greater column depth the K I lines are much more sensitive to pressure and therefore to surface gravity, whereas the weaker FeH and H₂O lines formed high in the atmosphere provide a better probe of rotational broadening.

G196-3B, the companion to the M2.5 G196-3A, is classified as an L2 dwarf (Kirkpatrick et al. 1999). The G196-3AB system is believed to be ~ 20 -300 Myr old, rather than the 1 Gyr thought to be typical of field L dwarfs (Rebolo et al. 1998). Figure 20 shows the order 61 spectrum of G196-3B plotted together with the L0.5 dwarf (2MASS 0746+20AB) and the L3.5 dwarf (2MASS 0036+18). Clearly, although the signal-to-noise ratio is poorer, all of the spectral features of G196-3B are much narrower than expected for an L2 dwarf. Using high resolution far-red optical spectra, Basri et al. (2000) measured 10 km s^{-1} for the rotational velocity of G196-3B. The infrared K I lines have cores only half as wide as those of the L0.5 and L3.5 dwarfs, and much less pronounced pressure-broadened line wings. This behavior suggests that the line profiles result primarily from lower surface gravity, consistent with the age of this object.

4.4. Metallicity effects

Burgasser et al. (2002) noted that the T6 dwarf 2MASS 0937+29 is peculiar because, despite having characteristics common to its spectral class, it appears to have no K I lines in a low-resolution *J*-band spectrum. If the K I lines were shallow and very broad, or sharp and weak, then they might escape detection at low spectral resolution. As shown in Figure 21 however, where we compare our high resolution spectrum of this T6 to that of the T4.5 dwarf 2MASS 0559–14, the K I lines are neither weak nor broad, they are completely absent.

Given the good signal-to-noise ratio of this high resolution spectrum, there is no possibility that the K I lines were simply too weak to detect.

Disappearance of the K I lines is unexpected because other T6 dwarfs still show these features (Burgasser et al. 2002, M03). In fact, we have observed the T5.5 2MASS 2356–15 which exhibits broad K I lines similar to those of a T5. Strong H₂O absorption features are clearly present in order 65 in the T6. These features show good correlation with the same features in the T4.5 but there is clear variation in the individual features. One possible reason for the absence of the K I lines in 2MASS 0937+29 is that this object has a different metallicity from other field dwarfs. Alternatively, the lines could be veiled by dust, but the trend at these spectral types is for dust to settle below the photosphere. In any case, there are other features in 2MASS 0937+29 that do not appear to be veiled.

2MASS 0937+29 was also classified as peculiar because of its extremely blue NIR colors and because it also has a very red optical spectrum for its type, as determined from CH₄ and H₂O strengths. This combination of attributes led Burgasser et al. (2002) to propose that 2MASS 0937+29 is an old, metal-poor brown dwarf in which enhanced collision-induced H₂ absorption in the *K*-band gives the unusual blue NIR color. If this is an old T dwarf then it is also probably a fairly high-mass brown dwarf that has cooled to the temperature of a T6, and consequently it has a higher gravity, higher pressure atmosphere. The higher gravity could also result in increased pressure broadening of the H₂O lines in 2MASS 0937+29 which would explain why these features seem muted and broader. In a recent study, Burgasser, Burrows and Kirkpatrick (2006) have found that the high surface gravity can result in a cooler effective temperature than equivalent T6 dwarfs. It is known (e.g., M03) that K I lines disappear around T7 or T8, hence it is possible that 2MASS 0937+29 is depleted in K I because of its low temperature rather than a low metallicity. Because the high-resolution spectra presented here show no residual trace of the K I lines, and because the H₂O lines are unusually broad, we contend that 2MASS 0937+29 must be cooler and/or more metal poor than a normal T6 dwarf.

5. Conclusions

Using a sequence of high-resolution infrared *J*-band spectra ($R \sim 20,000$ or 15 km s^{-1}) obtained with NIRSPEC on the Keck II telescope, we have studied the spectral morphology of objects from M6 to T6. The principal results of the survey are as follows:

- (1) Hundreds of small-scale spectral features are identified to be either FeH or H₂O

absorption features. Over ten times as many FeH features as previously identified in brown dwarf spectra are now confirmed. A few features of CrH are also identified, but no convincing transitions of TiO or CH₄ at J-band are found in this sample. FeH features attain maximum strength in the mid-L dwarfs, while H₂O absorption becomes steadily stronger towards later spectral types.

(2) FeH and H₂O line widths are typically $\sim 20 \text{ km s}^{-1}$ for the late M dwarfs, but broaden abruptly by over a factor of two at the M to L transition. We interpret this effect as evidence for increased rotational velocities in L dwarfs.

(3) The doublet of Al I at 1.31270 and 1.31543 μm is shown to be very sensitive to spectral type. This doublet weakens through M9 and then vanishes abruptly between M9 and L0. We suggest that this sudden disappearance is more a consequence of a transition in atmospheric chemistry than a simple decrease in atomic population levels resulting from a change in effective temperature. That is, the aluminum atoms are suddenly bound up into molecules and grains.

(4) The wings and line widths of the K I doublets at 1.16934, 1.17761 μm and at 1.24357, 1.25256 μm increase systematically, while line depth weakens with later spectral type. The equivalent width (W) of the K I features reaches a maximum in the mid-L dwarfs, decreases and then remains almost constant through T4.5. The K I line profiles begin to exhibit pressure broadened wings as early as late M. Line widths (FWHM) range from $\sim 50 \text{ km s}^{-1}$ at M5 to almost 500 km s^{-1} at T4.5. This effect is consistent with the much greater depth that is probed in cool T dwarf atmospheres at *J*-band.

(5) As shown in Figure 12, a characteristic of the transition from L to T dwarfs is the decay of FeH spectral structure, resulting in a smooth spectrum at high resolution for late L dwarfs and early T dwarfs, before H₂O dominant spectral structure develops.

(6) The young L2, G196-3B, exhibits very narrow K I lines without extensive pressure-broadened wings, indicative of a lower gravity atmosphere.

(7) Kelu-1AB, another L2, has exceptionally broad infrared lines, including FeH and H₂O features, confirming its status as a rapid rotator ($V \sin i \sim 60 \text{ km s}^{-1}$).

(8) Finally, the peculiar T6 dwarf 2MASS 0937+29 displays a complete absence of potassium, in contrast to other late T objects. We interpret this as either a metallicity effect (depletion of K atoms) or a cooler T_{eff} for this high surface gravity object.

Although the sample of objects of different spectral types is relatively small, these high-resolution, high signal-to-noise spectra of M, L and T dwarfs should provide an important benchmark for the detailed development and improvement of model atmospheres.

The authors wish to thank the staff of the Keck Observatory for their outstanding support. I.S.M. acknowledges the staff of the UCLA Infrared Laboratory and colleagues James Graham (UCB), James Larkin (UCLA) and Eric Becklin (UCLA) for their support throughout the development of the NIRSPEC instrument. We thank Adam Burrows, Katharina Lodders, Linda Brown, Didier Saumon, Richard Freedman, Travis Barman and Mark Marley for helpful discussions and opacity data. Finally, we thank the anonymous referee for a careful and complete critique of this paper. Work by S.S.K. was supported by the Astrophysical research Center for the Structure and Evolution of the Cosmos (ARCSEC) of Korea Science and Engineering Foundation through the Science Research Center (SRC) program. A.J.B. acknowledges support by NASA through Hubble Fellowship grant HST-HF-01137.01 awarded by the Space Telescope Science Institute, which is operated by the Association of universities for research in Astronomy, Inc., for NASA, under contract NAS 5-26555. This research has made use of the NASA/IPAC Infrared Science Archive, which is operated by the Jet Propulsion Laboratory, California Institute of Technology, under contract with the National Aeronautics and Space Administration. This publication makes use of data from the Two Micron All Sky Survey, which is a joint project of the University of Massachusetts and the Infrared Processing and Analysis Center, funded by the National Aeronautics and Space Administration and the National Science Foundation. Finally, the authors wish to extend special thanks to those of Hawaiian ancestry on whose sacred mountain we are privileged to be guests.

REFERENCES

- Auman, J., Jr., 1967, *ApJS*, 14, 171
- Basri, G. 2000, *ARA&A*, 38, 485
- Basri, G., Mohanty, S., Allard, F., Hauschildt, P. H., Delfosse, X., Martín, E. L., Forveille, T., & Goldman, B 2000, *ApJ*, 538, 363
- Becklin, E.E., & Zuckerman, B. 1988, *Nature*, 336, 656
- Bouy, H., Martín, E. L., Brandner, W., & Bouvier, J. 2005, *AJ*, 129, 511
- Burgasser, A. J., et al. 2000, *AJ*, 120, 1100
- Burgasser, A. J., et al. 2002, *ApJ*, 564, 421
- Burgasser, A. J., McElwain, M. W., Kirkpatrick, J. D., Cruz, K. L., Tinney, C. G. & Reid, I. N. 2004, *AJ*, 127, 2856

- Burgasser, A. J., Reid, I. N., Leggett, S. K., Kirkpatrick, J. D., Liebert, J. & Burrows, A. 2005, *ApJ*, 634, L177
- Burgasser, A. J., Geballe, T. R., Leggett, S. K., Kirkpatrick, J. D., & Golimowski, D. A. 2006, *ApJ*, 637, 1067
- Burgasser, A. J., Burrows, A., & Kirkpatrick, J. D. 2006, *ApJ*, 639, 1095
- Burrows, A., Hubbard, W. B., Lunine, J. I., & Liebert, J. 2001, *Rev. Mod. Phys.*, 73, 719
- Burrows, A., Ram, R.S., Bernath, P., Sharp, C.M. & Milsom, J.A. 2002, *ApJ*, 577, 986
- Burrows, A. & Voloyubev, M. 2003, *ApJ*, 583, 985.
- Clarke et al. 2003, *MNRAS*, 341, 239
- Cushing, M. C., Rayner, J. T., Davis, S. P., & Vacca, W. D. 2003, *ApJ*, 582, 1066
- Cushing, M. C., Rayner, J. T., & Vacca, W. D. 2005, *ApJ*, 623, 1115
- Delfosse, X., et al. 1997, *A & A*, 327, L25
- Delfosse, X., Tinney, C. G., Forveille, T., Epchtein, N., Borsenberger, J., Foque, P., Kimeswenger, S., Tiphene, D., 1999, *A & AS*, 135, 41
- Galehouse, D. C., Davis, S. P., & Brault, J. W. 1980, *ApJS*, 42, 241
- Geballe, T. R., Kulkarni, S. R., Woodward, C. E. & Sloan, G. C. 1996, *ApJ*, 467, L101
- Geballe, T. R., et al. 2002, *ApJ*, 564, 466
- Gelino, C. R., Kulkarni, S. R., & Stephens, D. C. 2006, *PASP*, 118, 611
- Golimowski, D. A., et al. 2004, *AJ*, 127, 3516
- Jones, H. R. A., Longmore, A. J., Jameson, R. F., & Mountain, C. M. 1994, *MNRAS*, 267, 413
- Jones, H. R. A., Longmore, A. J., Allard, F., & Hauschildt, P. H. 1996, *MNRAS*, 280, 77
- Kirkpatrick, J. D., Beichman, C. A., & Skrutskie, M. F. 1997, *ApJ*, 476, 311
- Kirkpatrick, J. D., et al. 1999, *ApJ*, 519, 802
- Kirkpatrick, J. D., et al. 2000, *AJ*, 120, 447
- Kirkpatrick, J. D., Dahn, C. C., Monet, D. G., Reid, I. N., Gizis, J. E., Liebert, J., & Burgasser, A. J. 2001, *AJ*, 121, 3235
- Kirkpatrick, J. D., Barman, T. S., Burgasser, A. J., McGovern, M. R., McLean, I. S., Tinney, C. G., & Lowrance, P. J. 2006, *ApJ*, 639, 1120
- Leggett, S. K., et al. 2000, *ApJ*, 536, L35

- Leggett, S. K., Allard, F., Geballe, T., Hauschildt, P. H., & Schweitzer, A. 2001, *ApJ*, 548, 908
- Liu, M.C. & Leggett, S.K., 2005, *ApJ*, 634, 616
- Lodders, K. 2002, *ApJ*, 577, 974.
- McGovern, M. R., Kirkpatrick, J. D., McLean, I. S., Burgasser, A. J., Prato, L., & Lowrance, P. J. 2004, *ApJ*, 600, 1020
- McLean, I. S., et al. 1998, *Proc. SPIE*, 3354, 566
- McLean, I. S., et al. 2000a, *ApJ*, 533, L45
- McLean, I. S., Graham, J. R., Becklin, E. E., Figer, D. F., Larkin, J. E., Levenson, N. A., & Teplitz, H. I. 2000b, *Proc. SPIE*, 4008, 1048
- McLean, I. S., Prato, L., Kim, S. S., Wilcox, M. K., Kirkpatrick, J. D., & Burgasser, A. 2001, *ApJ*, 561, L115
- McLean, I. S., McGovern, M. R., Burgasser, A. J., Kirkpatrick, J. D., Prato, L., Kim, S. S. 2003a, *ApJ*, 596, 561 (M03)
- McLean, I. S., McGovern, M. R., Prato, L., Burgasser, A. J., & Kirkpatrick, J. D. 2003b, in *Brown Dwarfs*, IAU Symp. 211, ed. E. Martín, ASP Conference Series.
- Mohanty, S., Basri, G., Jayawardhana, R., Allard, F., Hauschildt, P., & Ardila, D. 2004, *ApJ*, 609, 854
- Partridge, H., & Schwenke, D. W. 1997, *J. Chem. Phys.*, 106, 4618
- Phillips, J.G. 1973, *ApJS*, 26, 313
- Phillips, J.G., Davis, S.P., Lindgren, B., & Balfour, W.J. 1987, *ApJS*, 65,721
- Prato, L., Simon, M., Mazeh, T., McLean, I.S., Norman, D. & Zucker, S. 2002, *ApJ*, 569, 863
- Rebolo, R., Zapatero Osorio, M. R., Madrugá, S., Bejar, V. J. S., Arribas, S., Licandro, J., 1998, *Science*, 282,1309
- Reid, I. N., Kirkpatrick, J. D., Gizis, J. E., Dahn, C. C., Monet, D. G., Williams, R. J., Liebert, J., & Burgasser, A. J. 2000, *AJ*, 119, 369
- Reid, I. N., Kirkpatrick, J. D., Liebert, J., Gizis, J. E., Dahn, C. C., & Monet, D. G., 2002, *AJ*, 124, 519
- Ruiz, M. T., Leggett, S. K., & Allard, F. 1997, *ApJ*, 491, L107
- Saumon, D., Marley, M. S., Lodders, K., & Freedman, R. S.2003, in *Brown Dwarfs*, IAU Symp. 211, ed. E. Martín, ASP Conference Series.

- Schweitzer, A., Gizis, J. E., Hauschildt, P. H., Allard, F., & Reid, I. N. 2001, *ApJ*, 555, 368
- Simon, M., Bender, C., & Prato, L. 2006, *ApJ*, 644, 1183
- Testi, L., et al. 2001, *ApJ*, 522, L147
- Tokunaga, A. T. 2000, in *Allen’s Astrophysical Quantities*, ed. A. N. Cox (4th ed.; New York: Springer), 151
- Wilson, J. C., Kirkpatrick, J. D., Gizis, J. E., Skrutskie, M. F., Monet, D. G., & Houck, J. R. 2001, *AJ*, 122, 1989
- Zapatero Osorio, M. R., Lane, B. F., Pavlenko, Ya., Martín, E. L., Britton, M., & Kulkarni, S. R. 2004, *ApJ*, 615, 958
- Zapatero Osorio, M. R., Martín, E. L., Bouy, H., Tata, R., Deshpande, R., & Wainscoat, R. J. 2006, *ApJ*, 647, 1405

Table 1. **TARGET LIST, KEY PROPERTIES AND OBSERVING LOG**

Object	R.A. (J2000.0)	Dec. (J2000.0)	Spectral Type ^b	J^a (mag)	UT Date of Observation
G196-3A	10 04 21.0	50 23 06	M2.5	8.08±0.026	2002 Apr 23
Wolf 359 (GJ 406)	10 56 28.9	07 00 53	M6	7.09±0.024	2002 Apr 23
2MASSW J0140026+270150	01 40 02.6	27 01 50	M9	12.49±0.021	2000 Dec 4
2MASSP J0345432+254023	03 45 43.2	25 40 23	L0	14.00±0.027	2000 Dec 4
2MASSI J0746425+200032 ^c	07 46 42.6	20 00 32	L0.5	11.76±0.020	2002 Jan 1
Kelu-1 ^c	13 05 40.2	-25 41 06	L2	13.41±0.026	2003 May 12
G196-3B	10 04 21.0	50 23 06	L2	14.83±0.047	2002 Apr 23
2MASSW J0036159+182110	00 36 16.2	18 21 10	L3.5	12.47±0.027	2000 Dec 4
GD165B	14 24 39.1	09 17 10	L4	15.69±0.078	2003 May 13
2MASSW J1507476-162738	15 07 47.7	-16 27 39	L5	12.83±0.027	2000 Apr 25
DENIS-P J0205.4-1159 ^c	02 05 29.4	-11 59 30	L7	14.59±0.030	2001 Oct 9
SDSSp J042348.57-041403.5 ^c	04 23 48.6	-04 14 04	T0	14.47±0.027	2001 Oct 9
SDSSp J125453.90-012247.4	12 54 53.9	-01 22 47	T2	14.89±0.035	2003 May 14
2MASS J05591914-1404488	05 59 19.1	-14 04 48	T4.5	13.80±0.024	2001 Oct 9
2MASSI J2356547-155310	23 56 54.8	-15 53 11	T5.5	15.82±0.057	2005 July 19
2MASSI J0937347+293142	09 37 34.7	29 31 42	T6p	14.65±0.036	2003 May 12

^aFrom 2MASS All-Sky Point Source Catalog

^bSpectral types for L dwarfs are optical from Kirkpatrick et al. (1999, 2000, 2001); T dwarf spectral types are near-infrared from Burgasser et al. (2006).

^cKnown double or multiple object.

Table 2. **WAVELENGTH AND DISPERSION PROPERTIES OF THE *J*-BAND^a NIRSPEC ECHELLE ORDERS**

Order	Wavelengths (microns)	Interval (Å)	Dispersion (Å per pixel)	% Free Spectral Range
58	1.30447–1.32370	192.3	0.188	84.5
59	1.28262–1.30151	188.9	0.184	85.9
60	1.26137–1.27999	186.2	0.182	87.5
61	1.24081–1.25913	183.2	0.179	89.0
62	1.22093–1.23899	180.6	0.176	90.7
63	1.20168–1.21938	177.0	0.173	91.7
64	1.18293–1.20011	171.8	0.168	91.9
65	1.16496–1.18207	171.1	0.167	94.4

^aNIRSPEC-3 blocking filter ($\lambda\lambda$ 1.143-1.375 μm); echelle angle = 63.00 degrees; grating angle = 34.08 degrees.

Table 3. SPECTRAL FEATURES IN THE *J*-BAND NIRSPEC ECHELLE ORDERS

Feature	Wavelength ^a (μm)	Transition	Level Energy (eV)
Al I	1.3127007	4s $^2\text{S}_{1/2}$ - 4p $^2\text{P}_{3/2}$	3.143-4.087
Al I	1.3154345	4s $^2\text{S}_{1/2}$ - 4p $^2\text{P}_{1/2}$	3.143-4.085
CrH ^b	1.18?	6 bands of A ⁶ Σ^+ - X ⁶ Σ^+	...
Fe I	1.1693174	a ⁵ P ₁ - z ⁵ D ^o ₁	2.223-3.283
Fe I	1.1786490	b ³ P ₂ - z ³ D ^o ₃	2.831-3.884
Fe I	1.1886098	a ⁵ P ₂ - z ⁵ D ^o ₃	2.198-3.241
Fe I	1.1887337	a ⁵ P ₁ - z ⁵ D ^o ₂	2.223-3.266
Fe I	1.1976325	a ⁵ P ₃ - z ⁵ D ^o ₄	2.176-3.211
FeH ^c	1.1939 band head	0-1 band of F ⁴ Δ -X ⁴ Δ	...
FeH ^c	1.2389 band head	1-2 band of F ⁴ Δ -X ⁴ Δ	...
H ₂ O ^d	1.135	$\nu_1 + \nu_2 + \nu_3$...
H ₂ O ^d	1.331	2 ν_3 band	...
K I	1.1693420	4p $^2\text{P}_{1/2}$ - 3d $^2\text{D}_{3/2}$	1.610-2.670
K I	1.1772861	4p $^2\text{P}_{3/2}$ - 3d $^2\text{D}_{3/2}$	1.617-2.670
K I	1.1776061	4p $^2\text{P}_{3/2}$ - 3d $^2\text{D}_{5/2}$	1.617-2.670
K I	1.2435675	4p $^2\text{P}_{1/2}$ - 5s $^2\text{S}_{1/2}$	1.610-2.607
K I	1.2525560	4p $^2\text{P}_{3/2}$ - 5s $^2\text{S}_{1/2}$	1.617-2.607
Mn I	1.290329	a ⁶ D _{9/2} - z ⁶ P _{7/2}	2.114-3.075
Na I ^e	1.268261	3d $^2\text{D}_{5/2,7/2}$ - 5f $^2\text{F}_{5/2}$	3.617-4.595
Na I ^e	1.268269	3d $^2\text{D}_{3/2}$ - 5f $^2\text{F}_{5/2}$	3.617-4.595
Ti I	1.1896124	b ³ F ₂ - z ³ D ^o ₁	1.430-2.472
Ti I	1.2674567	b ³ F ₂ - z ³ F ^o ₃	1.430-2.408
Ti I	1.2834947	b ³ F ₂ - z ³ F ^o ₂	1.430-2.396
Ti I	1.2850544	b ³ F ₃ - z ³ F ^o ₃	1.443-2.408

^aAll wavelengths are vacuum; atomic wavelengths are from NIST.

^bBurrows et al. 2002

^cPhillips et al. 1987

^dAuman et al. 1967

^eBlended

Table 4. **1.2525 μm KI LINE PROPERTIES**

Spectral Type	Object	Line Depth	W (\AA)	FWHM (km s^{-1})
M2.5	G196-3A	0.36 ± 0.03	1.3 ± 0.4	39 ± 4
M6	Wolf 359	0.72 ± 0.01	5.2 ± 0.5	64 ± 6
M9	2MASS J0140+27	0.80 ± 0.01	7.5 ± 0.7	110 ± 11
L0	2MASS J0345+25	0.66 ± 0.02	9.3 ± 0.9	180 ± 18
L0.5	2MASS J0746+20AB	0.71 ± 0.01	11.5 ± 1.1	210 ± 21
L2	KelU-1AB	0.60 ± 0.02	14.1 ± 1.4	320 ± 32
L3.5	2MASS J0036+18	0.69 ± 0.02	14.4 ± 1.4	240 ± 24
L4	GD165B	0.80 ± 0.01	12.6 ± 1.3	230 ± 23
L5	2MASS J1507-16	0.68 ± 0.02	10.0 ± 1.0	240 ± 24
L7	DENIS J0205-11AB	0.47 ± 0.05	8.6 ± 1.3	290 ± 29
T0	SDSS J0423-04AB	0.47 ± 0.06	9.3 ± 1.4	240 ± 24
T2	SDSS J1254-01	0.60 ± 0.05	9.8 ± 1.5	270 ± 27
T4.5	2MASS J0559-14	0.41 ± 0.07	9.4 ± 1.4	490 ± 50

Table 5. **1.243 μm KI LINE PROPERTIES**

Spectral Type	Object	Line Depth	W (\AA)	FWHM (km s^{-1})
M2.5	G196-3A	0.24 \pm 0.04	1.3 \pm 0.1	47 \pm 5
M6	Wolf 359	0.65 \pm 0.02	5.6 \pm 0.6	65 \pm 7
M9	2MASS J0140+27	0.77 \pm 0.01	9.0 \pm 0.9	78 \pm 8
L0	2MASS J0345+25	0.61 \pm 0.02	11.5 \pm 1.2	220 \pm 22
L0.5	2MASS J0746+20AB	0.67 \pm 0.02	14.1 \pm 1.4	230 \pm 23
L2	Kelu-1AB	0.57 \pm 0.02	14.1 \pm 1.4	320 \pm 31
L3.5	2MASS J0036+18	0.63 \pm 0.02	11.4 \pm 1.1	290 \pm 29
L4	GD165B	0.75 \pm 0.01	14.0 \pm 1.4	150 \pm 15
L5	2MASS J1507-16	0.62 \pm 0.02	14.7 \pm 1.5	270 \pm 27
L7	DENIS J0205-11AB	0.36 \pm 0.06	8.2 \pm 1.2	390 \pm 39
T0	SDSS J0423-04AB	0.36 \pm 0.08	7.5 \pm 1.1	300 \pm 30
T2	SDSS J1254-01	0.49 \pm 0.06	7.9 \pm 1.2	260 \pm 26
T4.5	2MASS J0559-14	0.29 \pm 0.09	9.4 \pm 1.4	460 \pm 46

Table 6. **PROPERTIES OF THE 1.245 μm FeH AND 1.1752 μm H₂O FEATURES**

Spectral Type	Object	FeH Depth	H ₂ O Depth
M2.5	G196-3A	0.03±0.04	0.022±0.01
M6	Wolf 359	0.12±0.04	0.080±0.016
M9	2MASS J0140+27	0.17±0.04	0.140±0.029
L0	2MASS J0345+25	0.25±0.04	0.110±0.022
L0.5	2MASS J0746+20AB	0.29±0.04	0.100±0.02
L2	Kelu-1AB	0.15±0.04	0.110±0.022
L3.5	2MASS J0036+18	0.28±0.04	0.160±0.023
L4	GD165B	0.35±0.05	0.35 ±0.05
L5	2MASS J1507−16	0.23±0.04	0.220±0.044
L7	DENIS J0205−11AB	0.19±0.08	0.270±0.067
T0	SDSS J0423−04AB	0.08±0.07	0.280±0.055
T2	SDSS J1254−01	0.16±0.07	0.380±0.075
T4.5	2MASS J0559−14	0.06±0.09	0.620±0.093

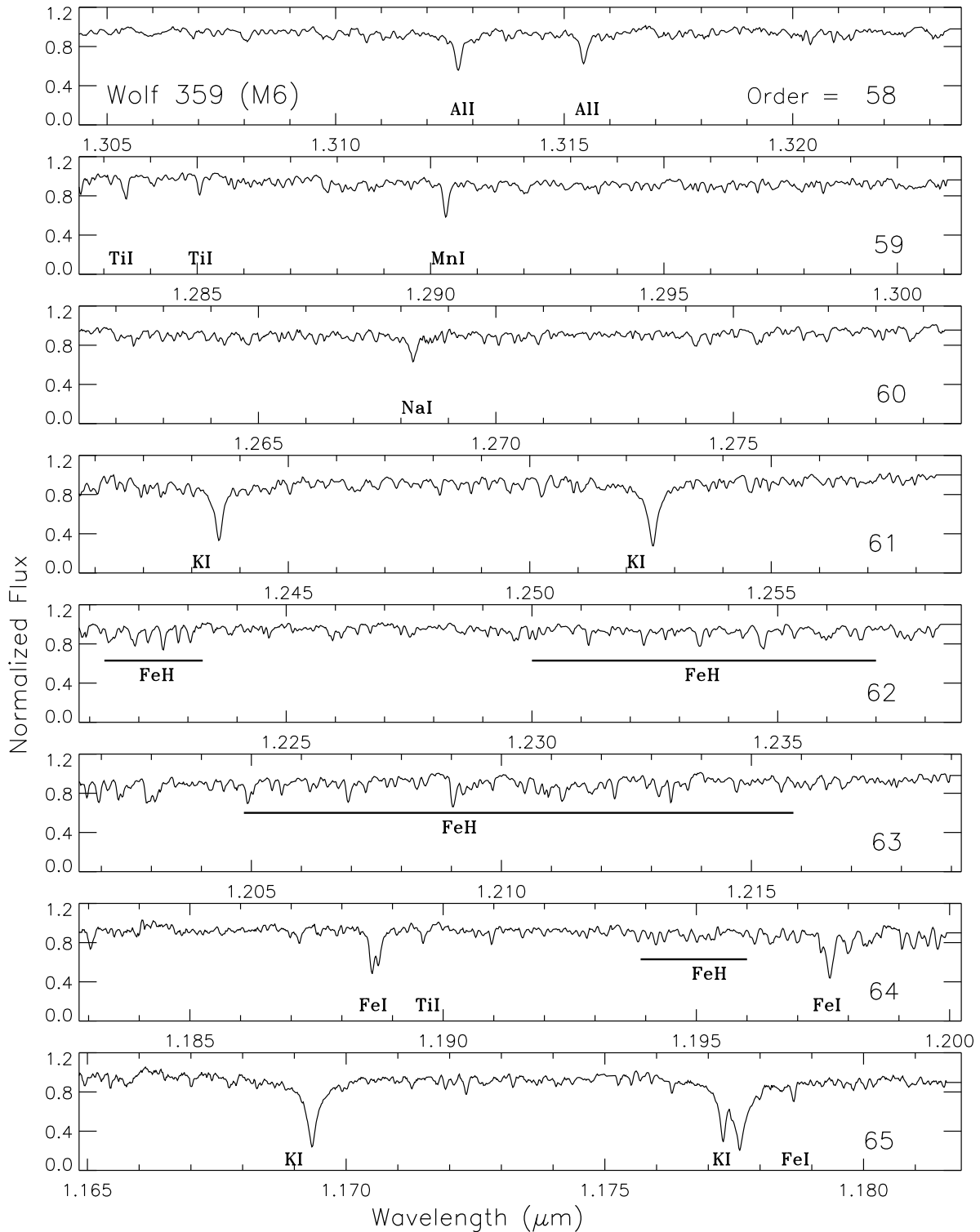


Fig. 1.— Eight NIRSPEC echelle orders covering the wavelength range 1.165–1.323 μm are shown for the M6 dwarf Wolf 359 (GJ 406). The resolving power is $\sim 20,000$ (15 km s^{-1}) giving a resolution of 0.625 \AA at $1.250 \mu\text{m}$. One pixel is $\sim 0.17 \text{ \AA}$ and wavelength tick marks are 10 \AA apart. Spectra are normalized to unity within each order, and shifted to the laboratory vacuum wavelengths. Key spectral features are labeled. The signal-to-noise ratio is close to 100:1. Essentially all of the fine spectral structure is real and repeatable; see text for details.

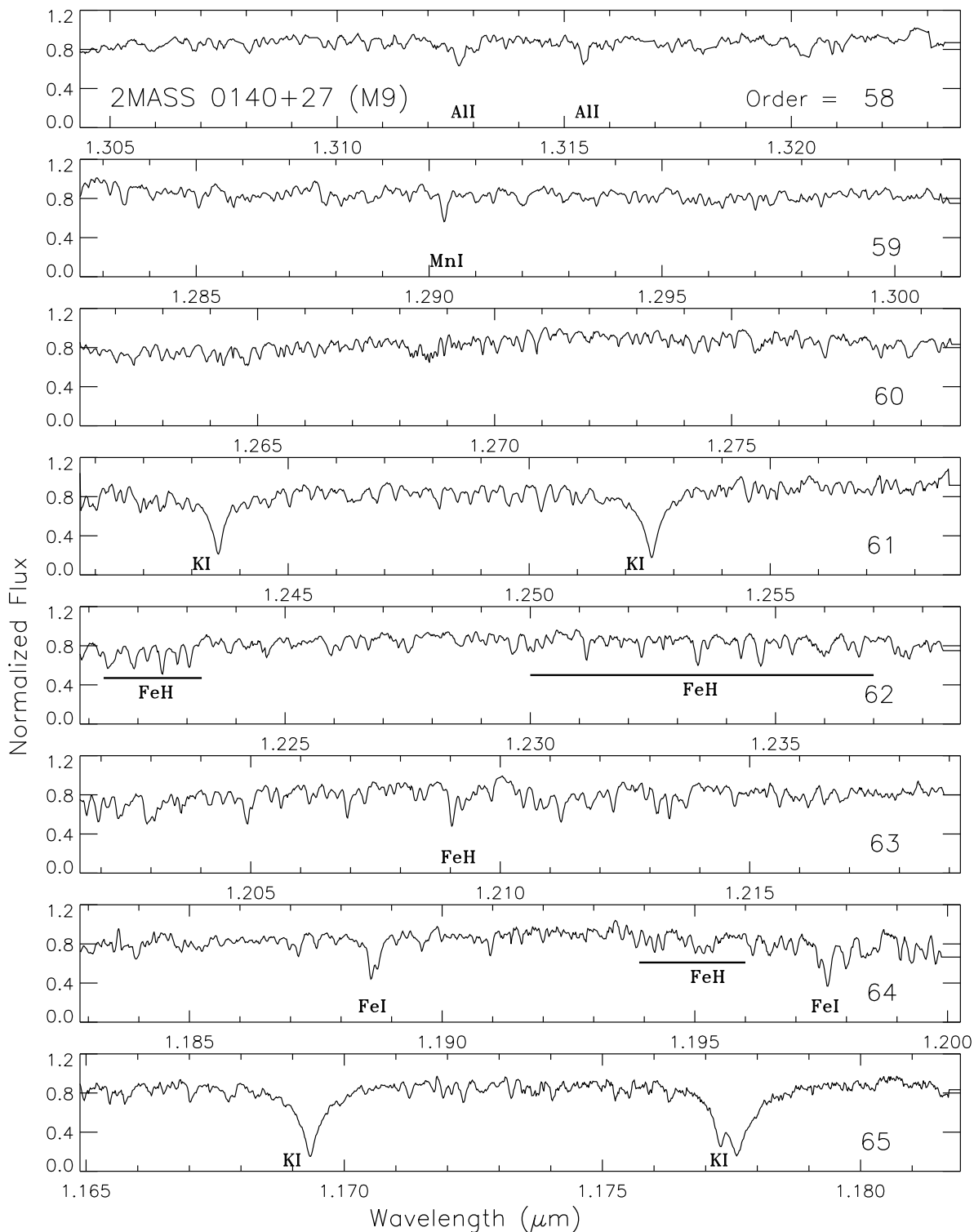


Fig. 2.— Eight NIRSPEC echelle orders covering the wavelength range 1.165-1.323 μm are shown for the M9 dwarf 2MASS 0140+27. As for Figure 1, the resolving power is $\sim 20,000$, the spectra are normalized to unity within each order and the spectra have been shifted to the laboratory vacuum wavelength scale. Key spectral features are labeled. The noise level ($\lesssim 2\%$) is almost imperceptible and the fine spectral structure is real and repeatable.

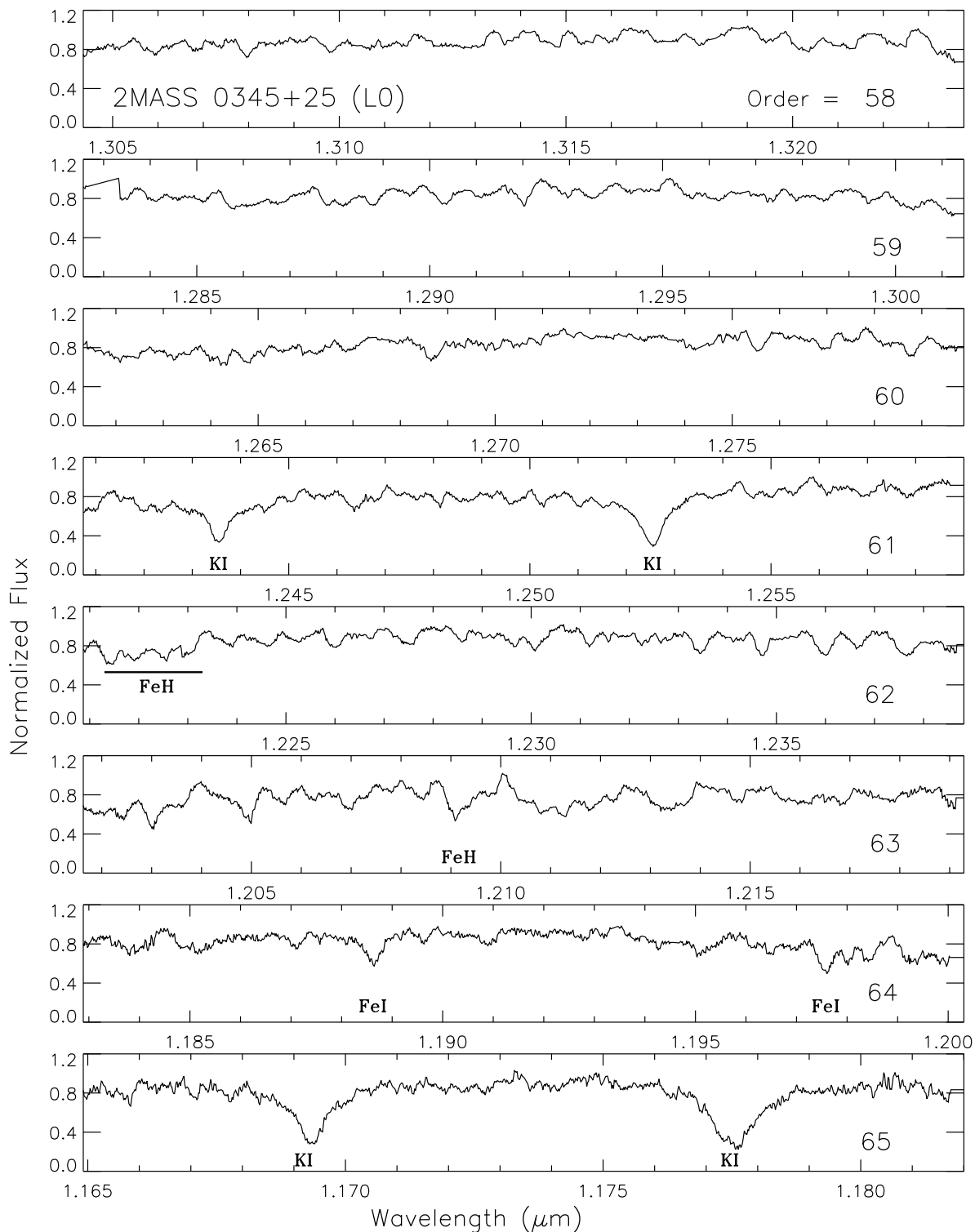


Fig. 3.— As for Figures 1 and 2, eight orders covering the wavelength range 1.165-1.323 μm are shown for the L0 dwarf 2MASS 0345+25. Spectra are normalized to unity within each order and shifted to laboratory vacuum wavelengths. Note the significant change in line widths; all features are broad. Key spectral features are labeled.

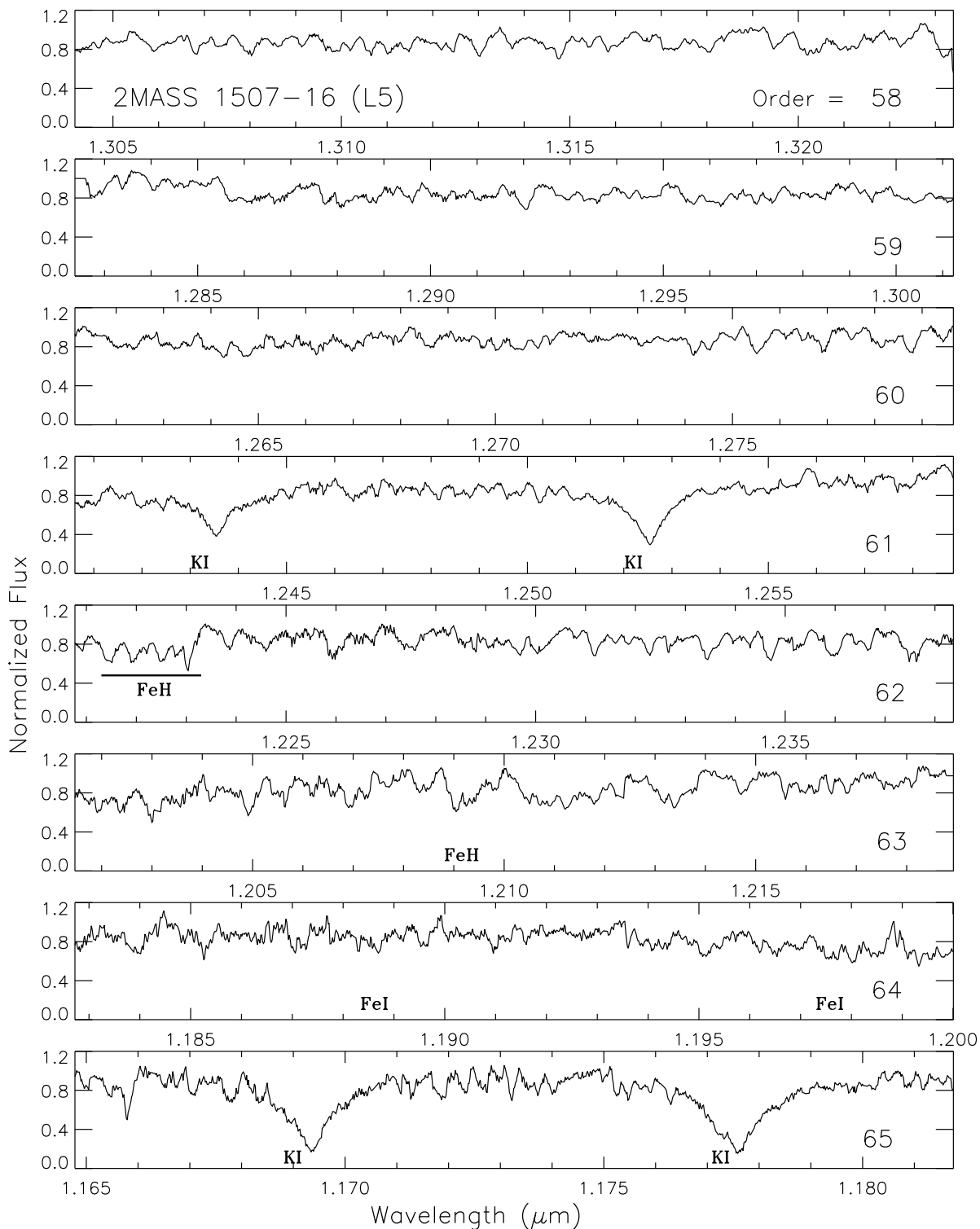


Fig. 4.— As for Figure 1-3, eight orders covering the wavelength range 1.165-1.323 μm are shown for the L5 dwarf 2MASS 1507-16. This spectrum is at a slightly lower resolving power than the other objects because a wider slit was used (see §2.1). Spectra are normalized to unity within each order and shifted to laboratory vacuum wavelengths. Key spectral features are labeled. The signal-to-noise ratio is better than 30:1 over most of the spectrum.

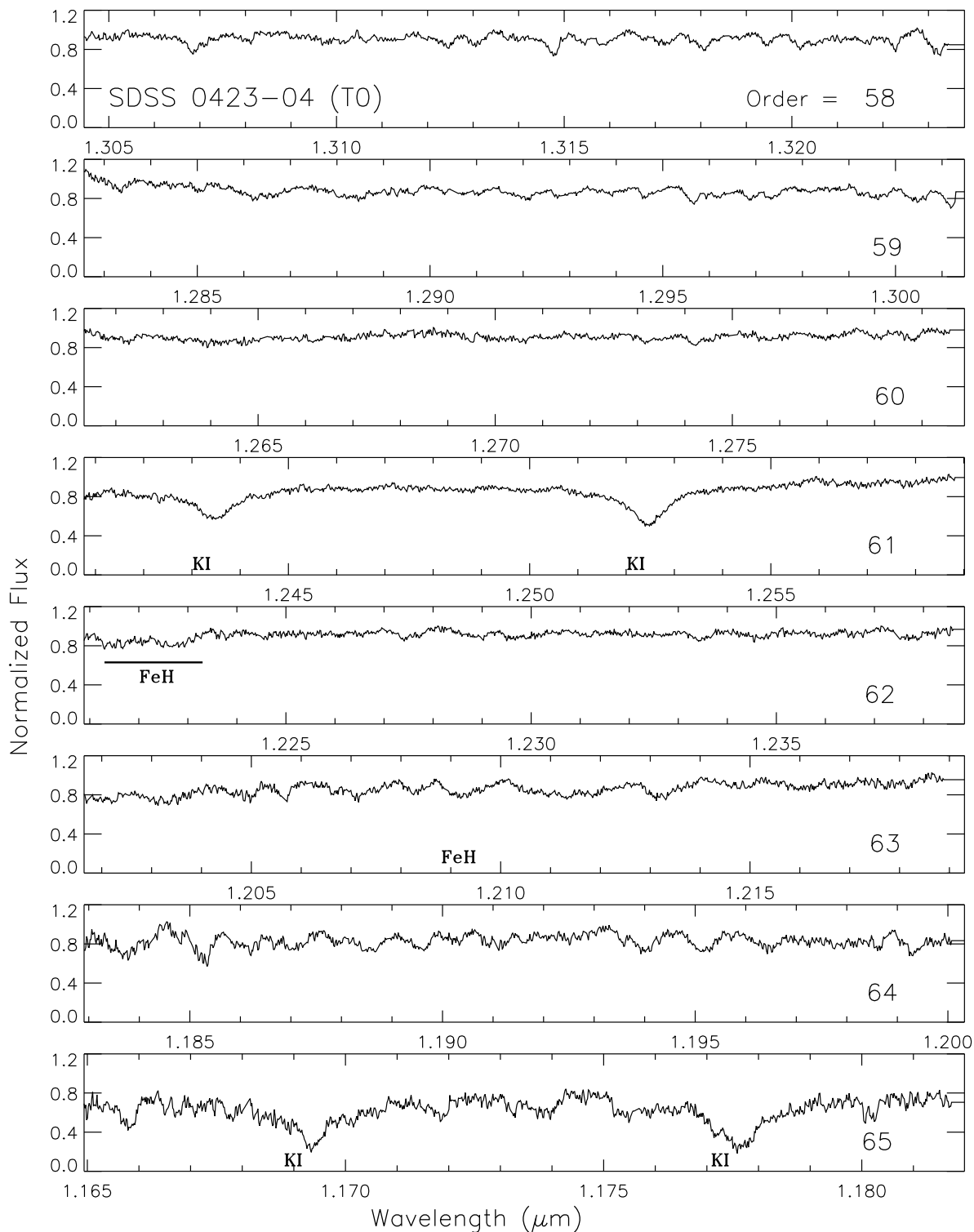


Fig. 5.— The same eight NIRSPEC echelle orders covering the wavelength range 1.165–1.323 μm as shown in Figures 1-4 are repeated here for the T0 dwarf SDSS 0423–04AB. The resolving power is $\sim 20,000$, spectra are normalized to unity within each order and vacuum laboratory wavelengths are used. Note how smooth the spectra have become relative to earlier spectral types. Key spectral features are labeled. The noise level is about 3-5% of the continuum.

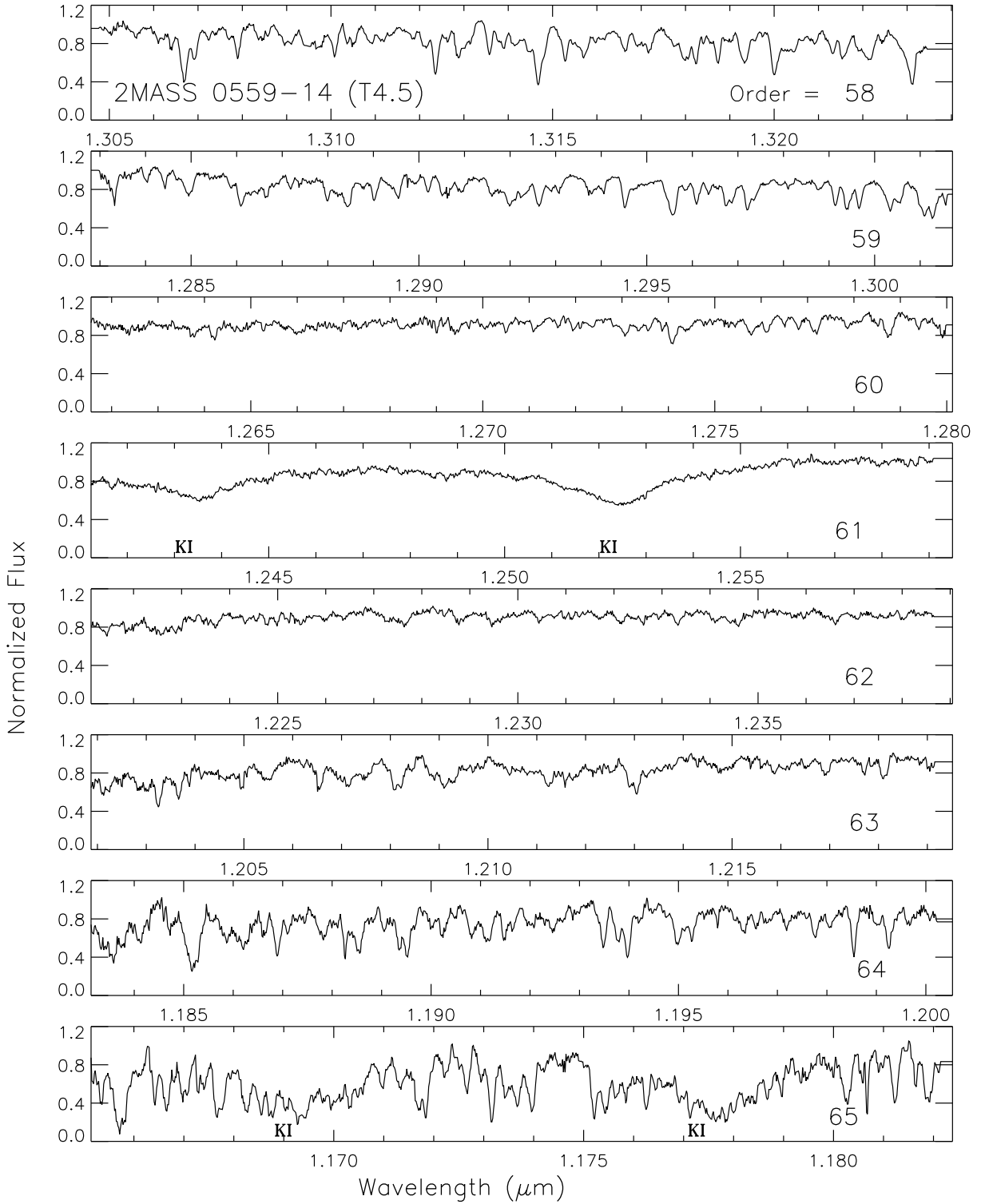


Fig. 6.— Eight orders covering the wavelength range 1.165-1.323 μm are shown for the T4.5 dwarf 2MASS 0559-14. As in the previous figures, the spectra have the same resolution, are normalized to unity within each order and shifted to vacuum laboratory wavelengths. Note the increase in absorption features, of H_2O , at both ends of the range. The noise level ($\lesssim 2\%$) is indicated by the smoothness in order 61.

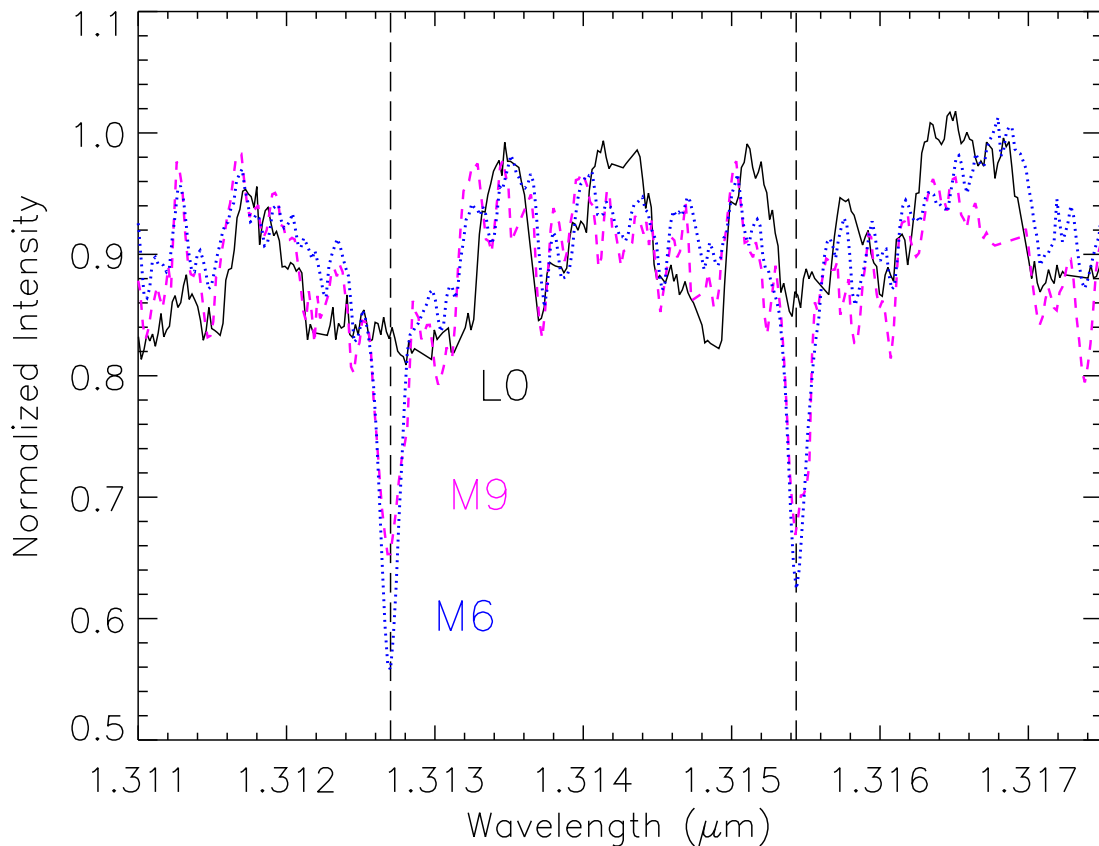


Fig. 7.— Part of the spectral region covered by order 58 containing the Al I doublet at 1.3127 and 1.3154 μm is compared for the M6 (Wolf 359; dotted), M9 (2MASS 0140+27; dashed) and L0 (2MASS 0345+25; solid) objects shown in Figures 1-3. The broad absorption features are due to blended H_2O transitions. All spectra are normalized to the same level and the intensity axis is plotted from 0.5 instead of zero for clarity of presentation. The Al I lines remain significant until M9 and then vanish abruptly between M9 to L0.

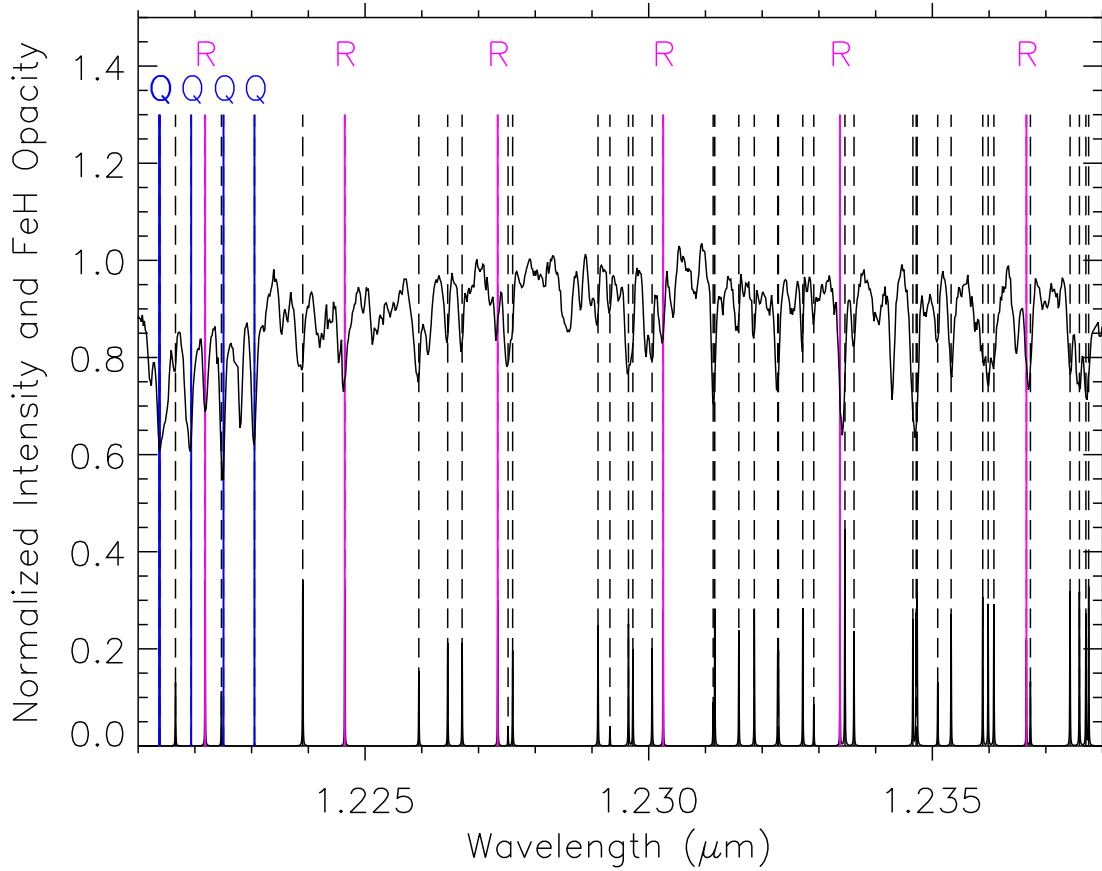


Fig. 8.— Order 62 from 1.221-1.238 μm for the M9 dwarf 2MASS 0140+27 is over-plotted on a scaled FeH opacity plot smoothed to $R \sim 20,000$. The region near 1.222 μm previously attributed to the Q-branch of the $F^4 \Delta_{7/2} - X^4 \Delta_{7/2}$ system of FeH is resolved, and almost every other feature is identified with P-branch (dotted vertical lines not otherwise labeled) or R-branch (labeled) lines of the 0–1 band. Lines not attributed to FeH are discussed in the text.

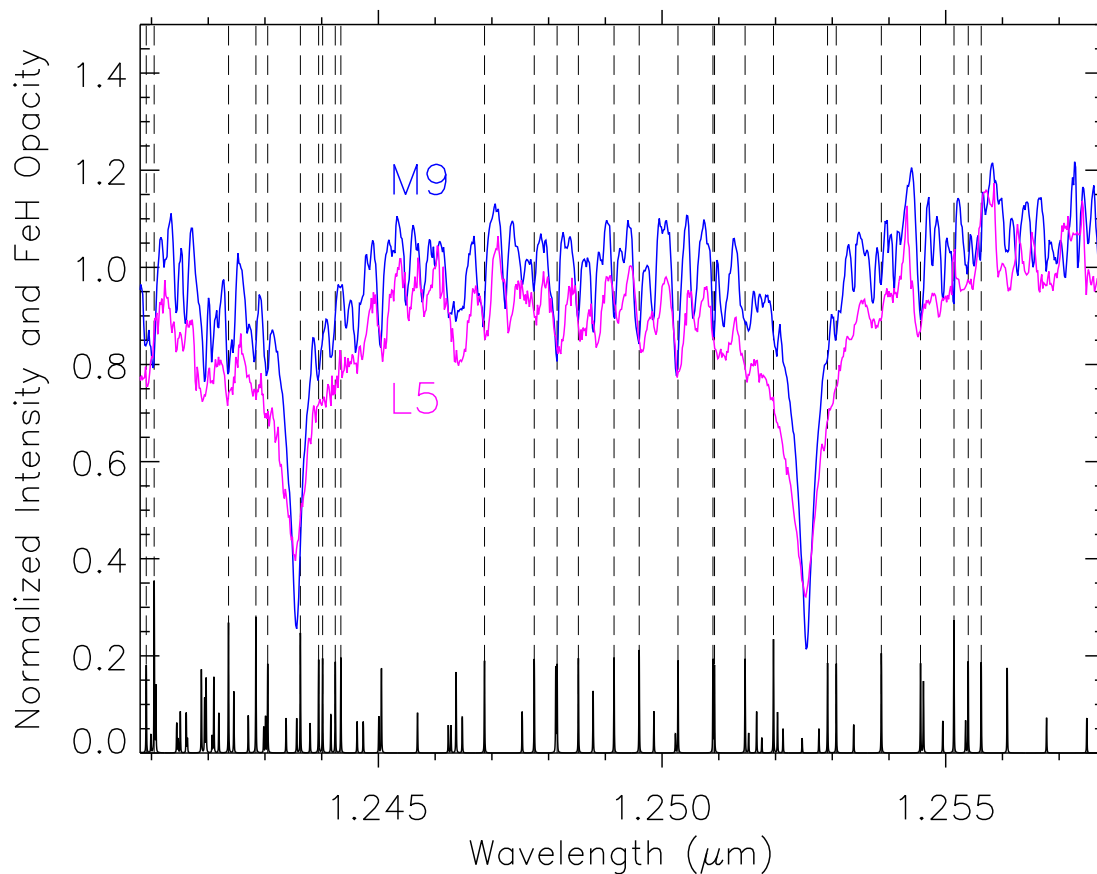


Fig. 9.— A plot of FeH opacity at 2000 K and a pressure of 1 bar, overlaid with the order 61 spectra of the M9 (2MASS 0140+27) and L5 (2MASS 1507–16) dwarfs from Table 1. Dashed lines show the location of the FeH transitions and the darker solid lines correspond to a resolution of $R \sim 20,000$. Although the features are broader in the L5 dwarf, almost all of the weaker features in order 61 can be attributed to FeH. Lines not attributed to FeH are discussed in the text. Note the broadening of the strong K I lines from M9 to L5.

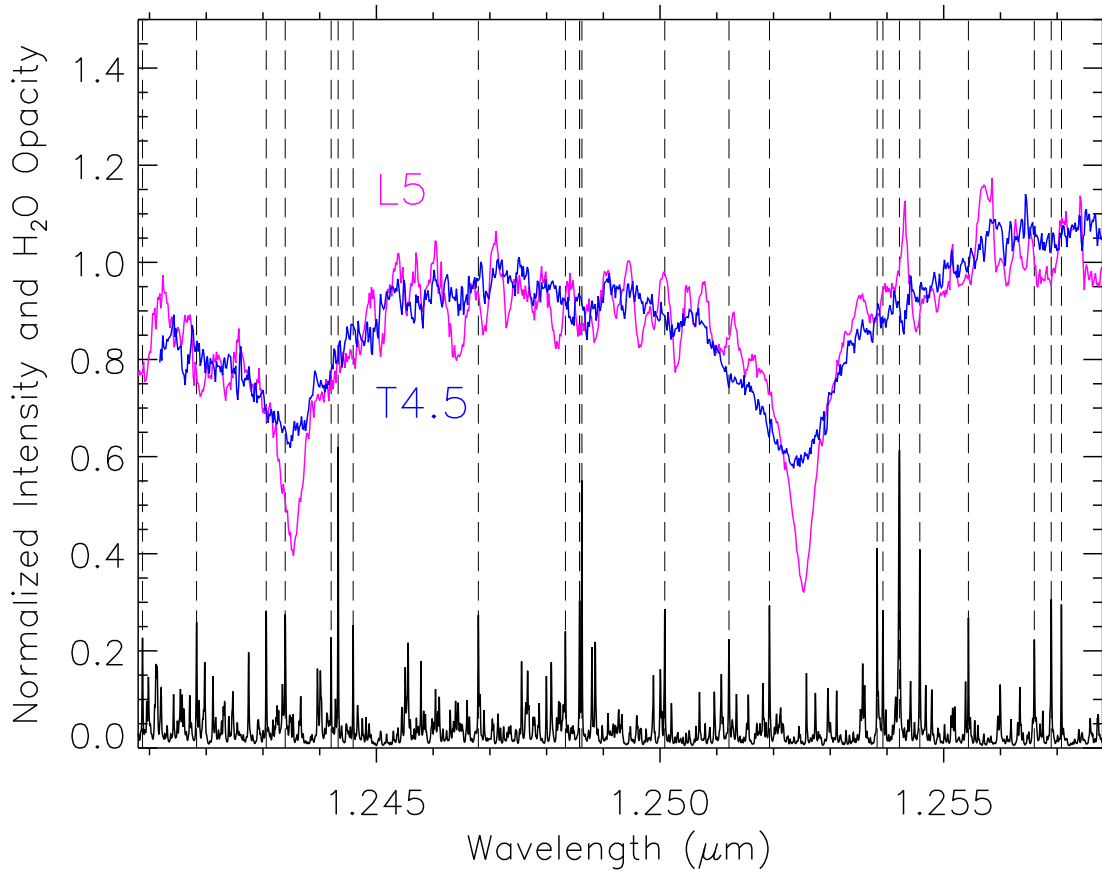


Fig. 10.— A plot of H_2O opacity at 1000 K and a pressure of 1 bar, is overlaid with the order 61 spectra of the L5 (2MASS 1507–16) and T4.5 (2MASS 0559–14) dwarfs from Table 1. Dashed lines show the location of the H_2O transitions and the solid lines correspond to a resolution of $R \sim 20,000$. H_2O features do not dominate either spectrum. Spectral features in the L5 that were not consistent with FeH cannot be attributed to H_2O . FeH is almost completely absent from the T4.5.

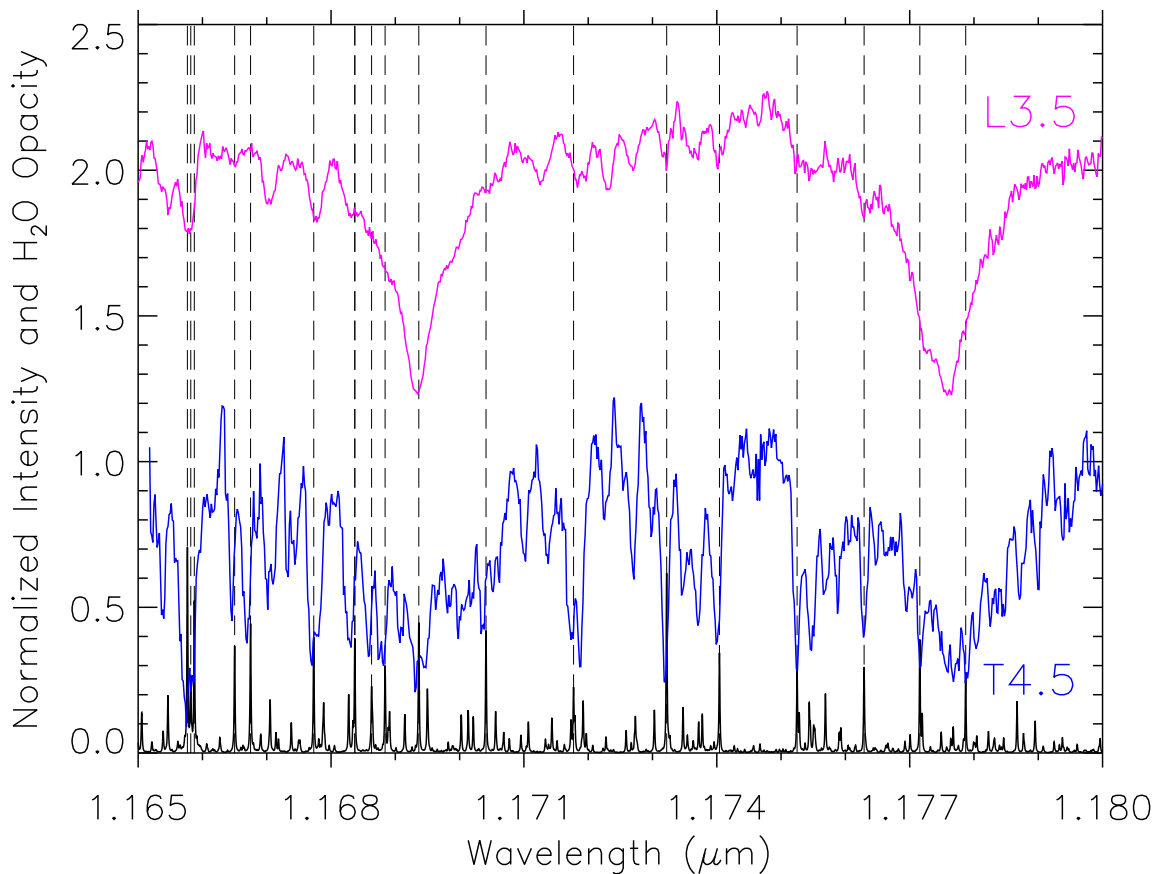


Fig. 11.— A plot of H_2O opacity at 1000 K and a pressure of 1 bar, overlaid with the order 65 NIRSPEC high-resolution spectra of the L3.5 (2MASS 0036+18) and T4.5 (2MASS 0559–14) dwarfs from Table 1. As in the previous figure, the solid lines correspond to a resolution of $R \sim 20,000$. No FeH lines are listed in the opacity tables for this order. All of the strong, sharper features in the T4.5 spectrum correlate well with H_2O transitions. For the L3.5 the correlation is weaker but still present. Note the broadening of the K I lines from L3.5 to T4.5.

Normalized Flux + Constant

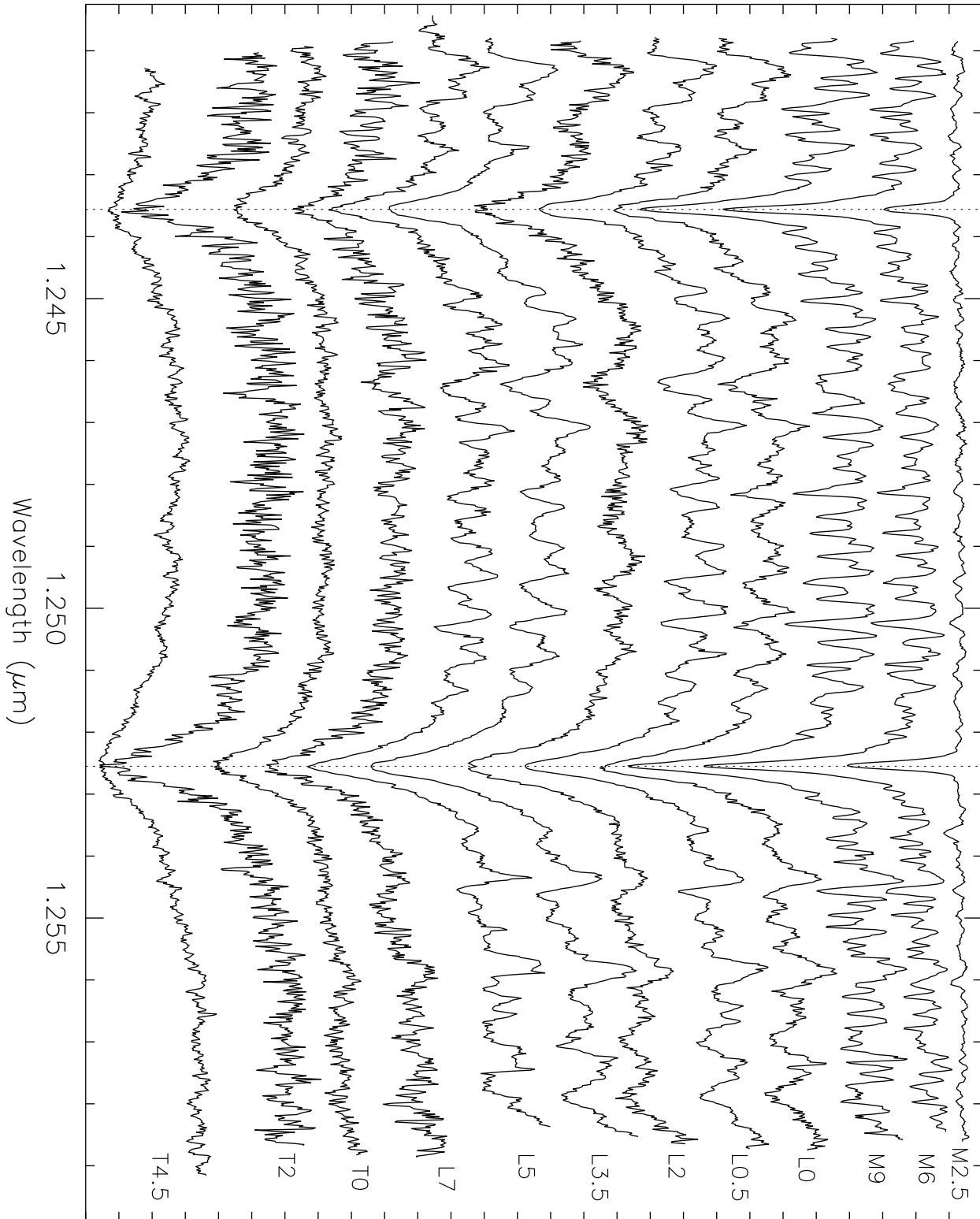


Fig. 12.— A spectral sequence of NIRSPEC echelle order 61 (1.241-1.258 μm) containing the longer wavelength K I doublet. Spectra are normalized to unity at peak flux and offset by a constant. Each spectrum has been shifted to the laboratory (vacuum) rest frame. The sequence of spectral types corresponds to Table 1; from top to bottom the range is M2.5 to T4.5. Note the presence in the M2.5 object of a very slight asymmetry in the position of the 1.25254 μm K I line that is not seen in the other K I line. This is due to blending with a Cr I line at 1.252527 μm , only 0.27 \AA to the blue.

Normalized Flux + Constant

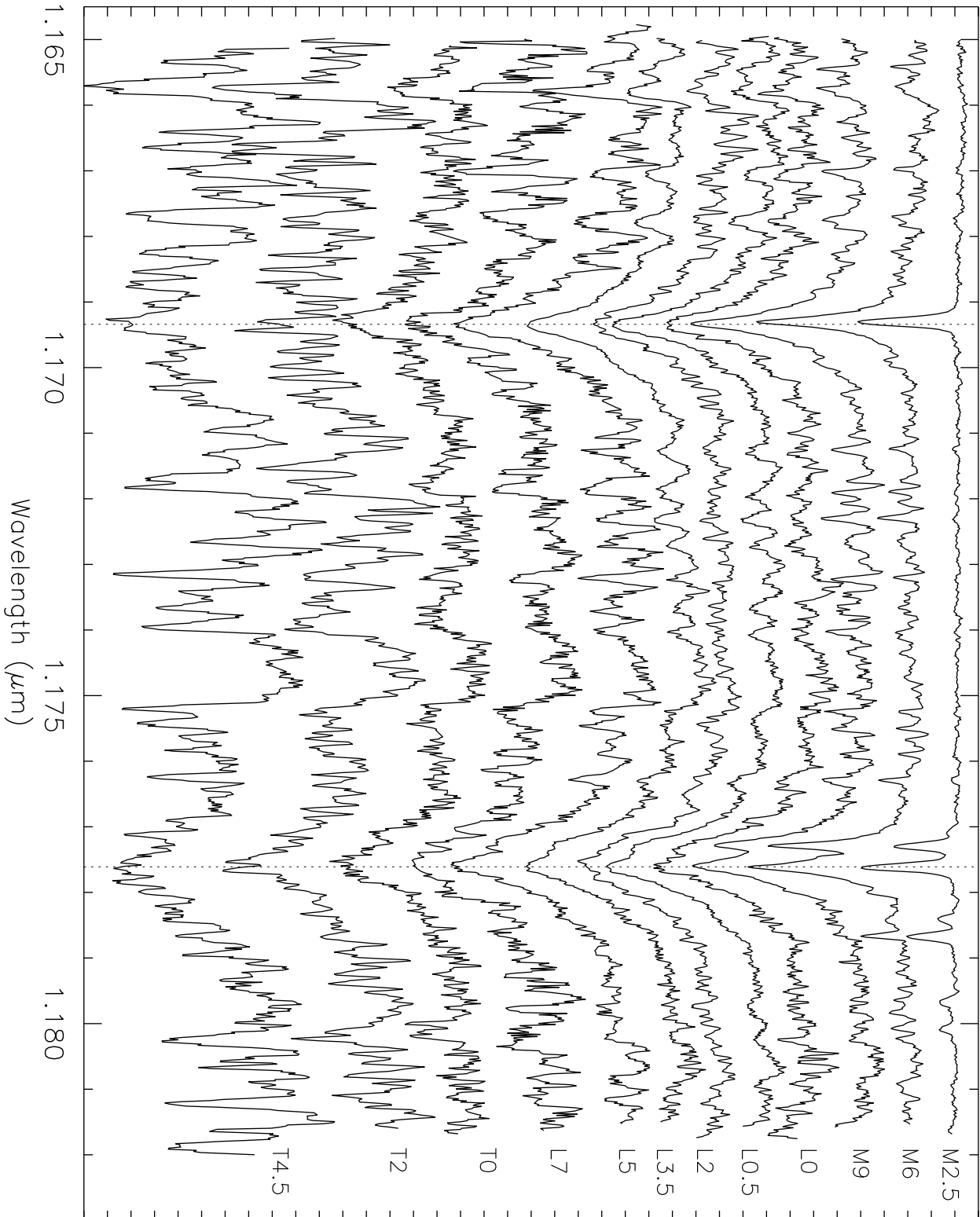


Fig. 13.— A spectral sequence of NIRSPEC echelle order 65 (1.165-1.181 μm) containing the shorter wavelength K I doublet. Spectra are normalized to unity and offset by a constant. Each spectrum has been shifted to the laboratory (vacuum) rest frame. The sequence of spectral types corresponds to Table 1; from top to bottom the range is M2.5 to T4.5.

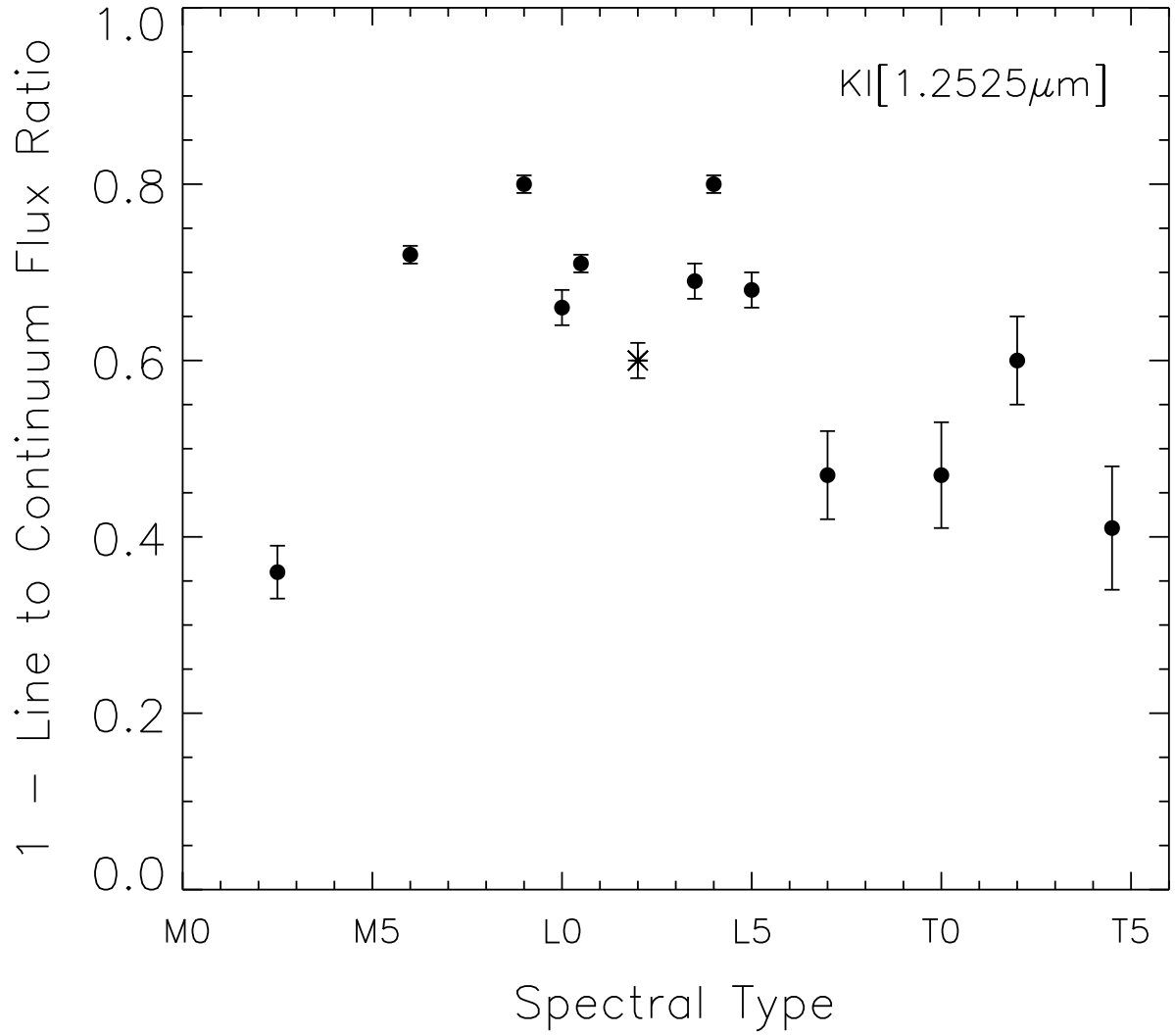


Fig. 14.— A plot of one minus the line to continuum flux ratio is used to measure the depth of the 1.2525 μ m K I line as a function of spectral type. For a very strong line the index approaches unity. The object indicated by the star symbol is Kelu-1AB.

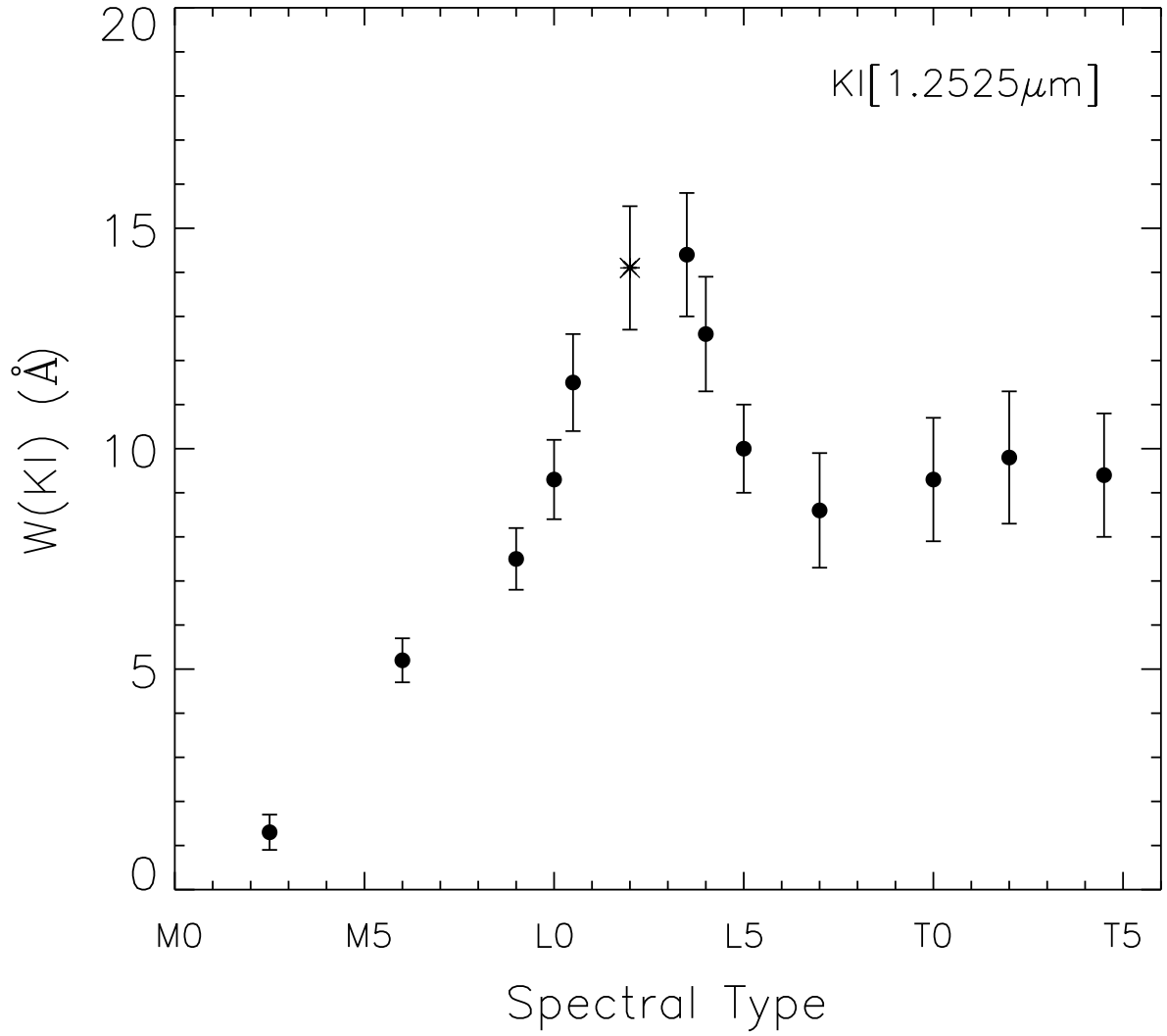


Fig. 15.— A plot of the equivalent width (W , in \AA) of the $1.2525 \mu\text{m}$ K I line as a function of spectral type. Error bars are estimated from a sequence of trial fits to the continuum. The object indicated by the star symbol is Kelu-1AB.

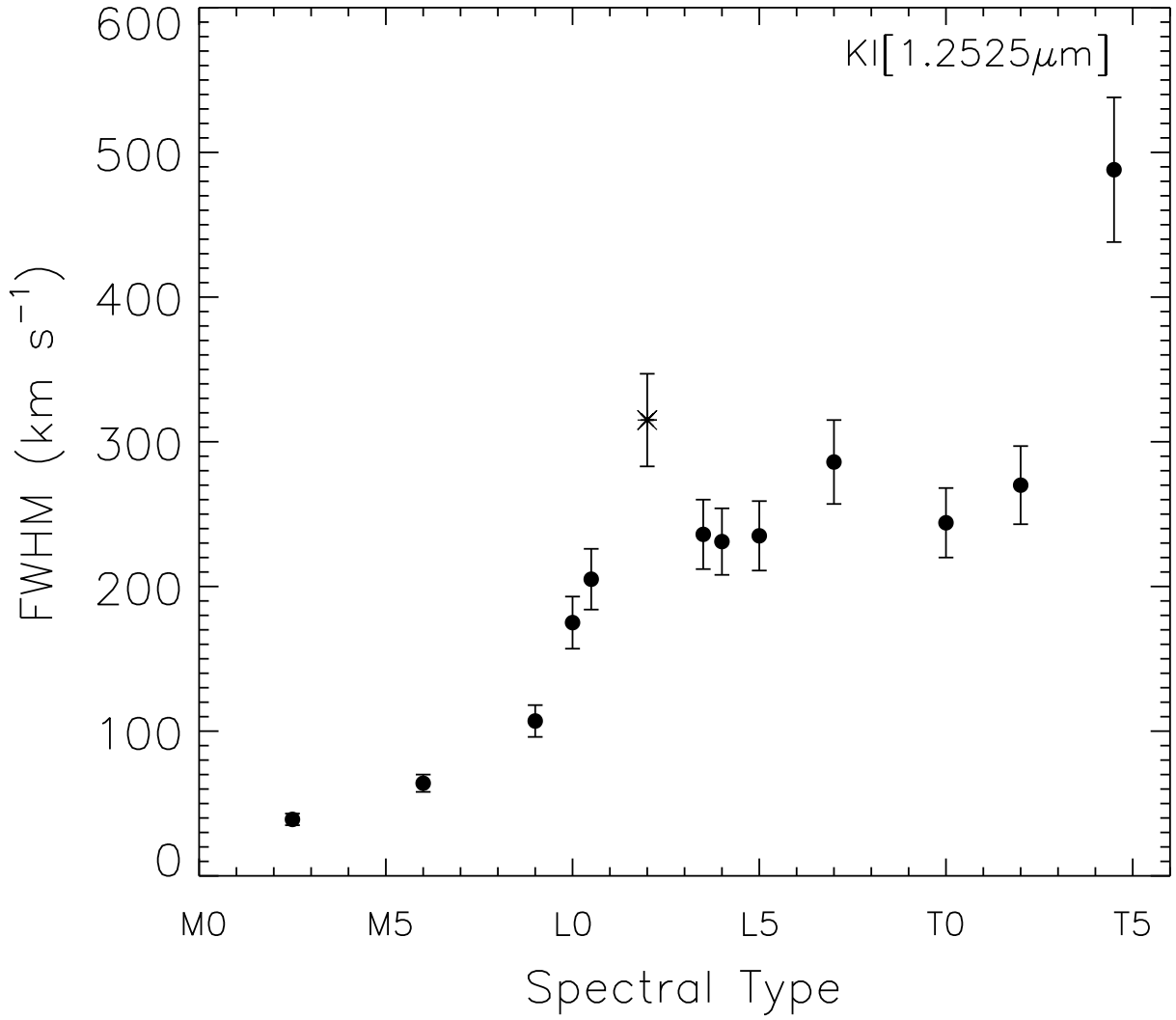


Fig. 16.— A plot of the FWHM (in km s⁻¹) of the 1.2525 μ m K I line as a function of spectral type. The object indicated by the star symbol is Kelu-1AB.

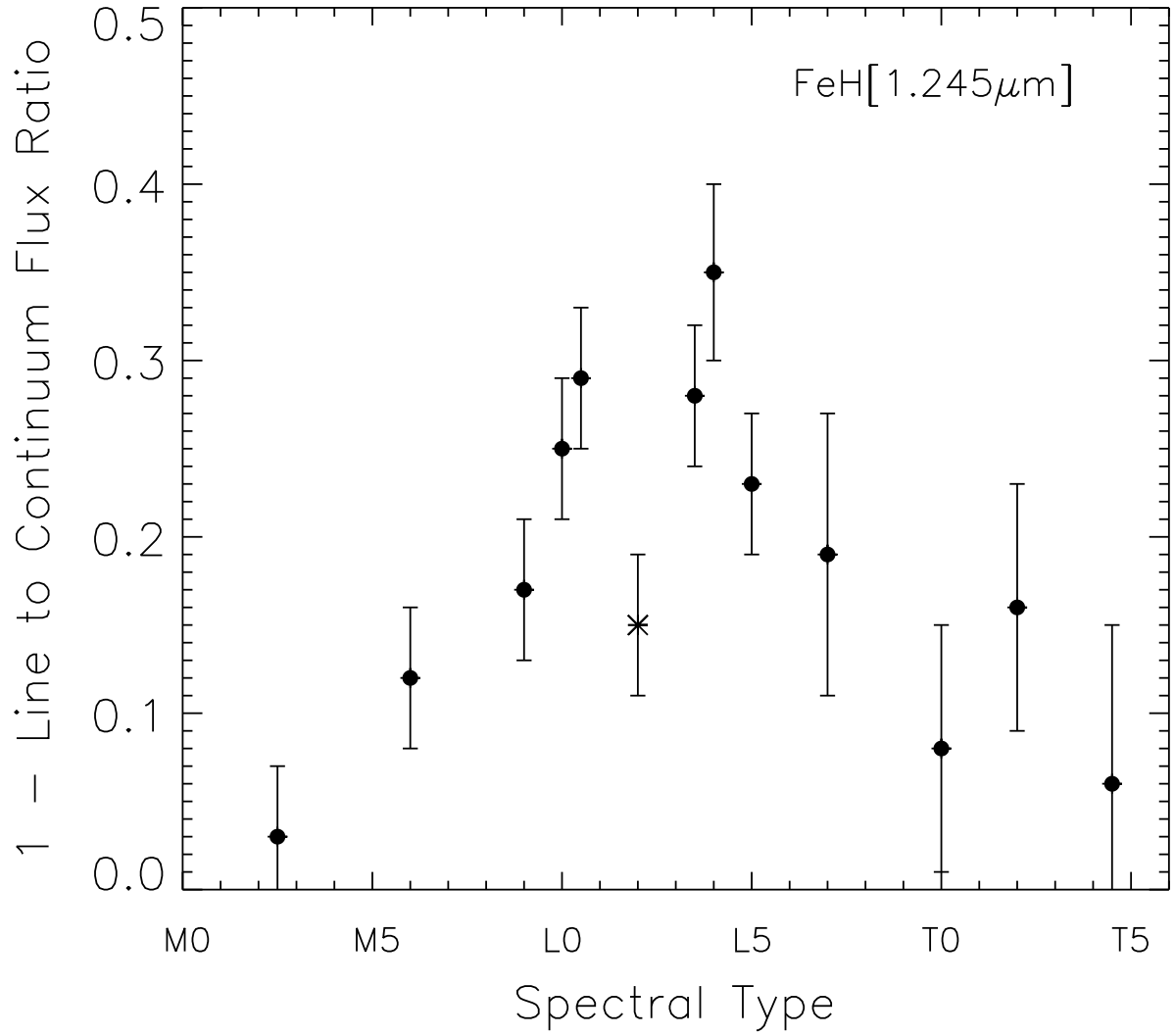


Fig. 17.— A plot of one minus the line to continuum flux for the strong FeH feature at 1.245 μ m as a function of spectral type. Again, the object indicated by the star symbol is Kelu-1AB which appears to be anomalous.

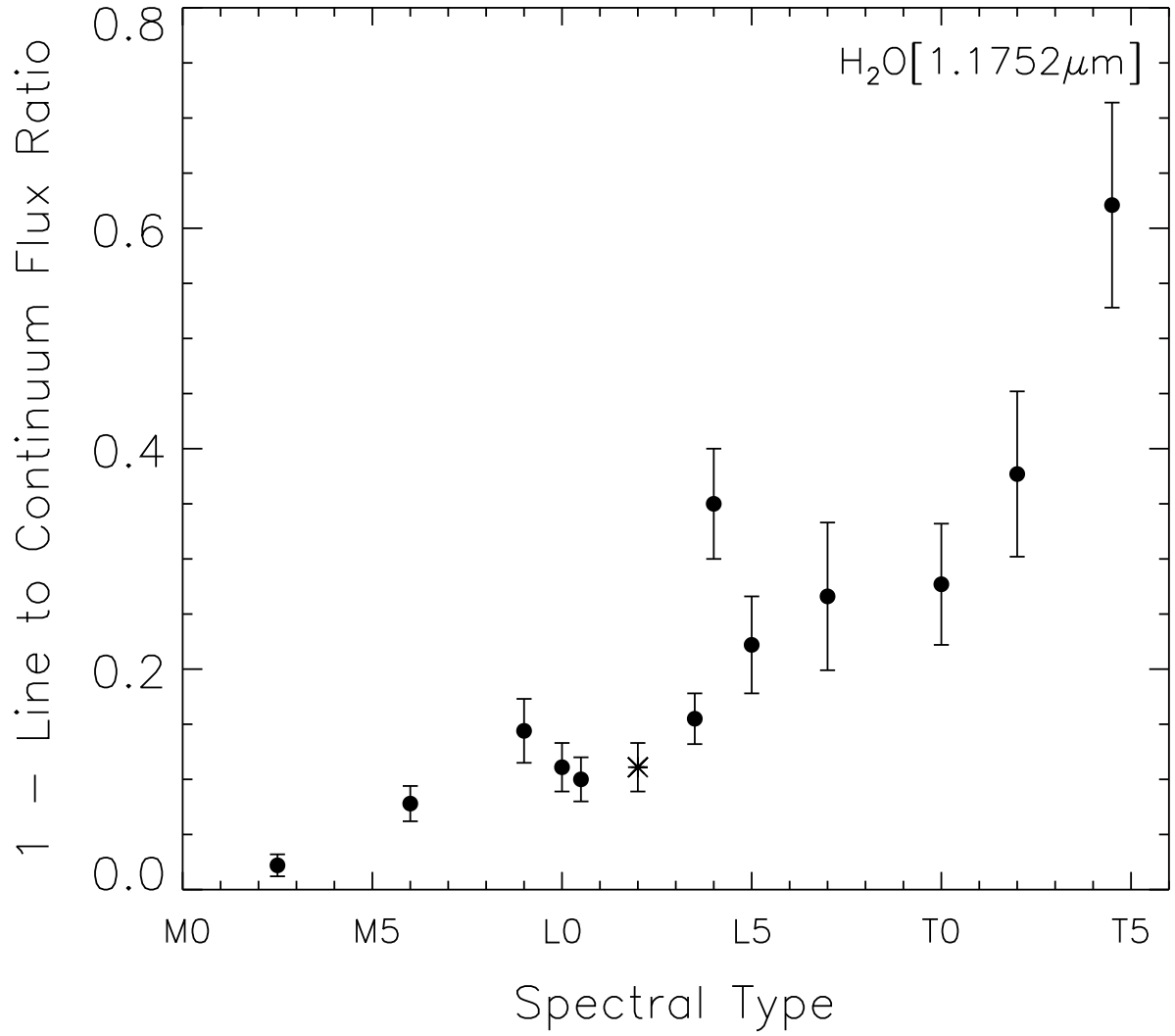


Fig. 18.— A plot of one minus the line to continuum flux ratio for the strong H₂O feature at 1.1752 μ m as a function of spectral type. As before, the object indicated by the star symbol is Kegu-1AB. In this plot it is GD165B (L4) that appears slightly above the general trend.

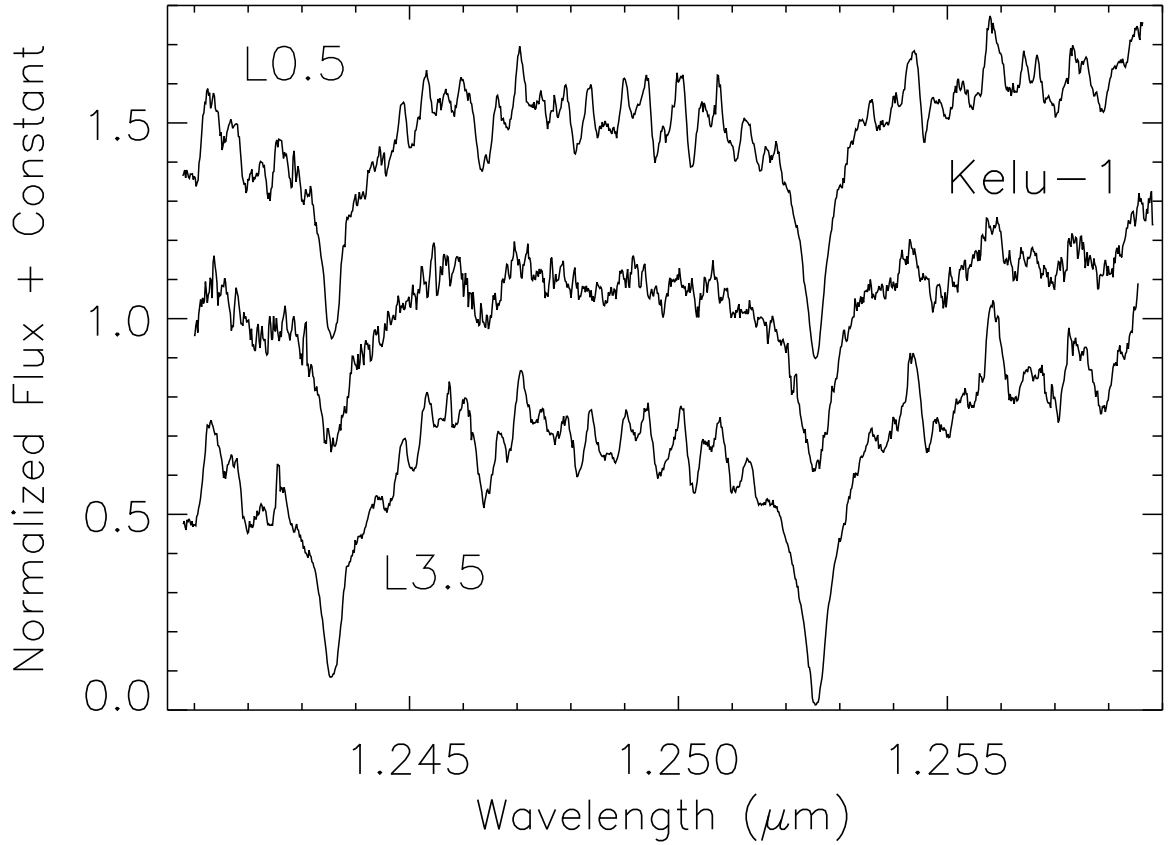


Fig. 19.— The high resolution spectrum at $1.25 \mu\text{m}$ (order 61) of the L2 dwarf Kelu-1AB compared to L0.5 and L3.5 dwarfs (2MASS 0746+20AB and 2MASS 0036+18, respectively). The K I lines are significantly broader and shallower in Kelu-1AB, even compared to the binary L0.5. Spectra are normalized to unity and offset by a constant. Each spectrum has been shifted to the laboratory (vacuum) rest frame.

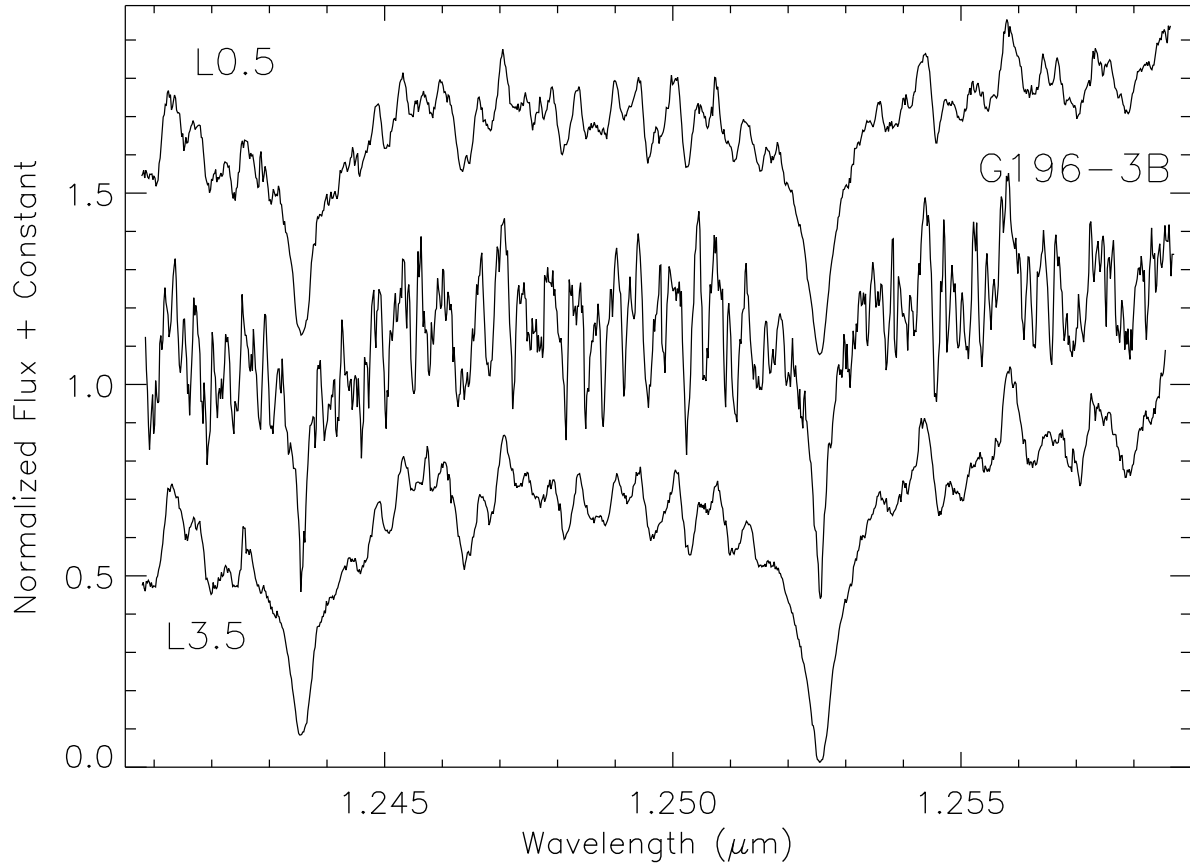


Fig. 20.— The high resolution spectrum at $1.25 \mu\text{m}$ (order 61) of the young L2 companion G196-3B compared to field L0.5 and L3.5 dwarfs (2MASS 0746+20AB and 2MASS 0036+18, respectively). The K I lines are significantly weaker and narrower. Spectra are normalized to unity at peak flux and offset by a constant. Each spectrum has been shifted to the laboratory (vacuum) rest frame.

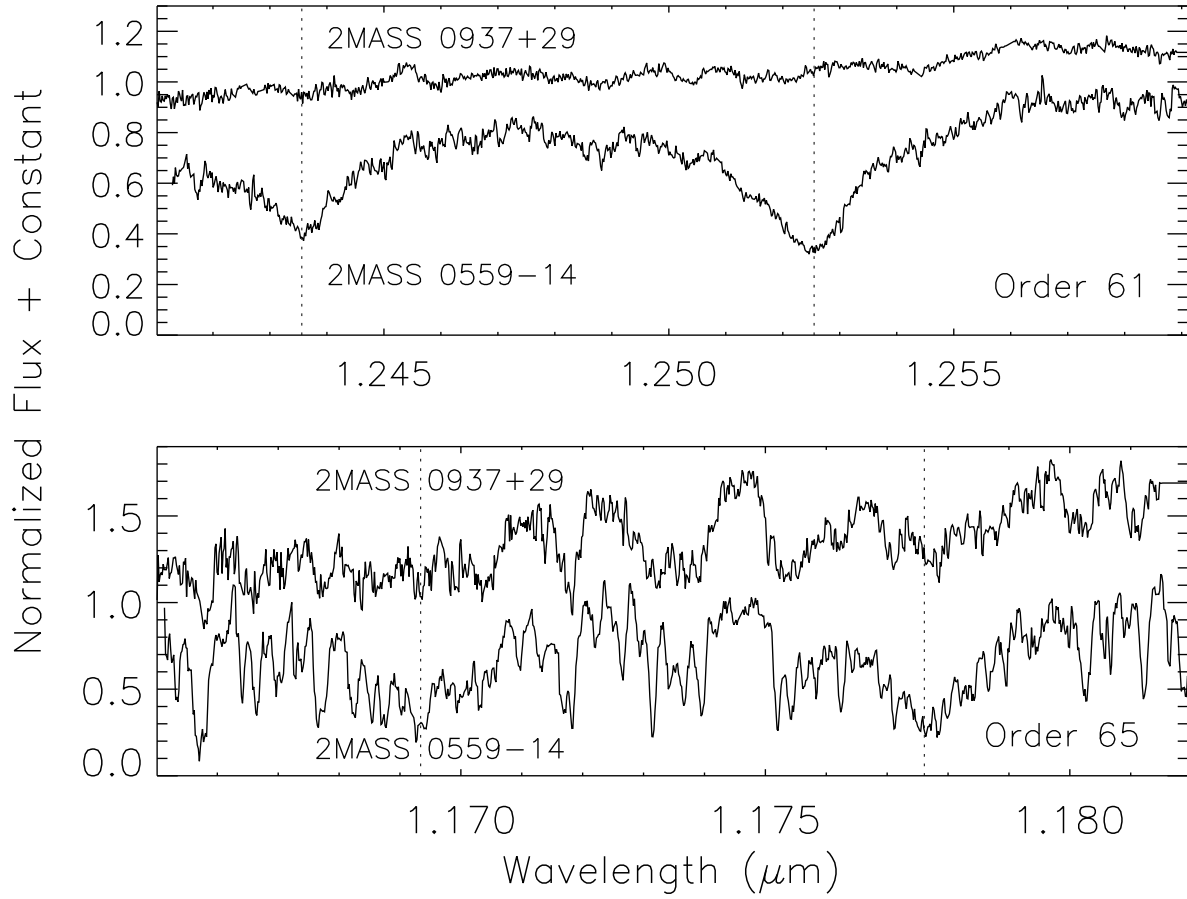


Fig. 21.— The high resolution spectra at $1.25 \mu\text{m}$ (order 61) and $1.173 \mu\text{m}$ (order 65) of the peculiar T6 dwarf 2MASS 0937+29 compared to that of the T4.5 dwarf 2MASS 0559–14. The K I lines are completely absent in both orders. Transitions due to H_2O in order 65 are present but muted in the peculiar T6.